# Augmin prevents merotelic attachments by promoting proper arrangement of bridging and kinetochore fibers

Valentina Štimac[1#], Isabella Koprivec[1#], Martina Manenica[1], Juraj Simunić[1], Iva M. Tolić[1*]

[1]Division of Molecular Biology, Ruđer Bošković Institute, Bijenička cesta 54, 10000 Zagreb, Croatia

[#]These authors contributed equally to this work.

*Corresponding author: I.M.T. (tolic@irb.hr)

**SUMMARY**

Štimac, Koprivec et al. show that augmin promotes mitotic fidelity and tension on kinetochores by generating parallel assemblies consisting of bridging fibers that connect sister kinetochore fibers, precise organization of which prevents erroneous attachments.

**ABSTRACT**

The human mitotic spindle is made of microtubules nucleated at centrosomes, at kinetochores, and from pre-existing microtubules by the augmin complex. However, it is unknown how the augmin-mediated nucleation affects distinct microtubule bundles and thereby mitotic fidelity. Here we use superresolution microscopy to analyze the previously indistinguishable microtubule arrangements within the crowded metaphase plate area and demonstrate that augmin is vital for the formation of uniformly arranged parallel units consisting of sister kinetochore fibers connected by a bridging fiber. This ordered geometry helps both prevent and resolve merotelic attachments through joint action of bridging and kinetochore fibers. Augmin depletion resulted in thinning of both kinetochore and bridging fibers, with bridging fibers often absent from kinetochore pairs with a reduced interkinetochore distance. We propose a model where augmin promotes mitotic fidelity and tension on kinetochores by generating assemblies consisting of bridging and kinetochore fibers that align sister kinetochores parallel to the spindle axis to face opposite poles, thereby preventing erroneous attachments.

## INTRODUCTION

The mitotic spindle has a sophisticated architecture that enables it to accurately segregate chromosomes during cell division. It consists of three major classes of microtubules: kinetochore microtubules that form kinetochore fibers (k-fibers) connecting chromosomes to the spindle pole through kinetochores, midplane-crossing microtubules that form antiparallel arrays in the central part of the spindle, and astral microtubules that extend from the spindle poles towards the cell cortex (McIntosh, 2016; O'Toole et al., 2020; Prosser and Pelletier, 2017). During metaphase and early anaphase, the majority of midplane-crossing microtubule bundles are laterally attached to a pair of sister k-fibers resembling a bridge between them, which is why they are called bridging fibers (Kajtez et al., 2016; Vukušić et al., 2017). These fibers balance the tension between sister kinetochores and maintain the curved shape of the metaphase spindle (Kajtez et al., 2016; Polak et al., 2017; Tolić and Pavin, 2016). In addition to linking sister k-fibers, some midplane-crossing microtubules can also form connections between neighboring k-fibers (O'Toole et al., 2020).

Spindle microtubules in human somatic cells are generated by several nucleation mechanisms, including centrosome-dependent and augmin-dependent nucleation (Kirschner and Mitchison, 1986; Pavin and Tolić, 2016; Petry, 2016; Prosser and Pelletier, 2017; Wu et al., 2008; Zhu et al., 2008), with an addition of chromatin- and kinetochore-dependent nucleation as a third mechanism that contributes to the directional formation of k-fibers (Maiato et al., 2004; Sikirzhytski et al., 2018; Tulu et al., 2006). Centrosome-dependent nucleation was long thought to be predominant in spindle assembly, however, numerous studies revealed that a significant number of microtubules also arise from pre-existing microtubules, through augmin, an eight-subunit protein complex that serves as a recruiter of the γ-tubulin ring complex (γ-TuRC) required for microtubule nucleation (David et al., 2019; Goshima et al., 2008; Kamasaki et al., 2013; Lawo et al., 2009; Song et al., 2018; Uehara et al., 2009). Augmin-nucleated microtubules grow at an angle of 0-30$^{o}$ relative to the pre-existing microtubule (Kamasaki et al., 2013; Petry et al., 2013; Verma and Maresca, 2019) and show a directional bias towards kinetochores, resulting in the preserved polarity of the spindle once the initial kinetochore-microtubule attachments form (David et al., 2019; Kamasaki et al., 2013). Depletion of augmin complex in different cell types results in impairment of microtubule bundles within the spindle accompanied by the formation of long, curved bundles on the spindle periphery, loss of spindle bipolarity, shorter interkinetochore distance, chromosome misalignment, mitotic delays, and a higher incidence of aneuploidy and cytokinesis failure (Almeida et al., 2022; Hayward et al.,

2014; Uehara and Goshima, 2010; Uehara et al., 2009; Wu et al., 2008; Zhu et al., 2008). Of the eight subunits in the complex, the two directly interacting subunits HAUS6 (hDgt6/FAM29A) and HAUS8 (hDgt4/Hice1) have been extensively studied because of their ability to interact with a γ-TuRC adapter protein NEDD1 and pre-existing microtubules, respectively (Song et al., 2018; Uehara et al., 2009). While previous studies mainly focused on the effect of augmin on astral and kinetochore microtubules, the effect on midplane-crossing microtubules remains largely unexplored (Almeida et al., 2022; Hayward et al., 2014; Song et al., 2018; Uehara et al., 2009, 2016; Uehara and Goshima, 2010; Wu et al., 2008; Zhu et al., 2008). Recent electron tomography work on spindles in human cells showed that ends of midplane-crossing microtubules interact with the wall of kinetochore microtubules (O'Toole et al., 2020), indicating that augmin-dependent nucleation might play an important role in their formation.

Augmin depletion has previously been linked to higher incidence of segregation errors (Wu et al., 2008) and the appearance of lagging chromosomes (Almeida et al., 2022; Viais et al., 2021), which were connected to impaired brain development in a recent study (Viais et al., 2021). Homozygous loss of HAUS6 subunit of the augmin complex was also seen in several cancer types, such as sarcomas, pancreatic adenocarcinomas, gliomas and glioblastomas (ICGC/TCGA, 2020, retrieved by using cBioPortal (Cerami et al., 2012; Gao et al., 2013)). However, the origin of segregation errors in augmin depletion remains largely unexplored due to extensive mitotic delays often experienced by these cells (Wu et al., 2008).

To explore how the augmin-dependent microtubule nucleation affects functionally distinct microtubule bundles and thereby mitotic fidelity, we depleted augmin in hTERT-RPE1 and HeLa cells and imaged them using stimulated emission depletion (STED) (Hell and Wichmann, 1994; Klar and Hell, 1999) and confocal microscopy. We show that the augmin complex plays a vital role in the formation of a highly organized metaphase plate area required for mitotic fidelity. Augmin depletion leads to a three-fold increase in segregation errors when the checkpoint is weakened. A significant number of lagging chromosomes following augmin depletion have a reduced tension and a large tilt with respect to the spindle axis in metaphase, which may facilitate the formation of merotelic attachments within the disorganized spindle area of augmin-depleted cells. The appearance of severely disordered microtubules occurs along with the strong reduction in the number of proper bridging microtubules connecting sister k-fibers. Interestingly, the interkinetochore distance after augmin depletion was larger for kinetochore pairs with bridging fibers than for those without, indicating a specific effect of the

augmin-generated bridging fibers on interkinetochore tension. Taken together, we propose that augmin affects mitotic fidelity by forming highly organized microtubule arrangements consisting of two sister k-fibers connected by a bridging fiber oriented parallel to the spindle axis, which are required to jointly regulate the kinetochore tension and prevent erroneous kinetochore-microtubule attachments during metaphase.

## RESULTS

### Augmin is vital for the formation of uniformly arranged units consisting of two sister k-fibers connected by a bridging fiber

To overcome the limitations of confocal microscopy and explore the relationship between different classes of microtubules within the crowded metaphase plate area, we performed stimulated emission depletion (STED) superresolution imaging (Hell and Wichmann, 1994; Klar and Hell, 1999) of microtubules within the bipolar metaphase spindles of human cells (Fig. 1A-B, Supplementary Fig. S1). This enabled us to easily distinguish between k-fibers that start at kinetochores and midplane-crossing microtubules that pass through the central part of the spindle. HAUS6 or HAUS8 components of the augmin complex were depleted by siRNA in hTERT-RPE1 (hereafter referred to as RPE1) cells stably expressing CENP-A-GFP and immunostained for tubulin (Fig. 1A, Supplementary Fig. S1). Augmin depletion was confirmed using immunocytochemistry and Western blot analysis (Supplementary Fig. S2A-C).

In control cells, the vast majority of midplane-crossing microtubule bundles laterally attached to a pair of sister k-fibers and formed a bridging fiber between them, consistent with previous findings (Kajtez et al., 2016; Vukušić et al., 2017). These bridging fibers were nearly-parallel with respect to one another and the spindle axis. Additionally, a small portion of midplane-crossing microtubules formed a secondary connection between a k-fiber on one side and a non-sister k-fiber on the other side (O'Toole et al., 2020). In comparison with untreated cells, midplane-crossing microtubules after HAUS6 or HAUS8 depletion extended at a variety of angles, and were wavy and disordered, particularly in the inner part of the spindle close to the pole-to-pole axis. Strikingly, midplane-crossing microtubules less often formed bridging fibers that connect to sister k-fibers in cells depleted of HAUS6 or HAUS8. Instead, they formed more complex arrangements, primarily consisting of one or more connections between various k-fibers within the metaphase spindle. This was contrary to k-fibers which, even though often missing a bridge between them, appeared relatively similar to those in control cells (Fig. 1B,

Supplementary Fig. S1). Taken together, augmin is vital for the proper organization of midplane-crossing microtubules into uniformly arranged bridging fibers that connect two sister k-fibers and extend nearly-parallel to the spindle axis.

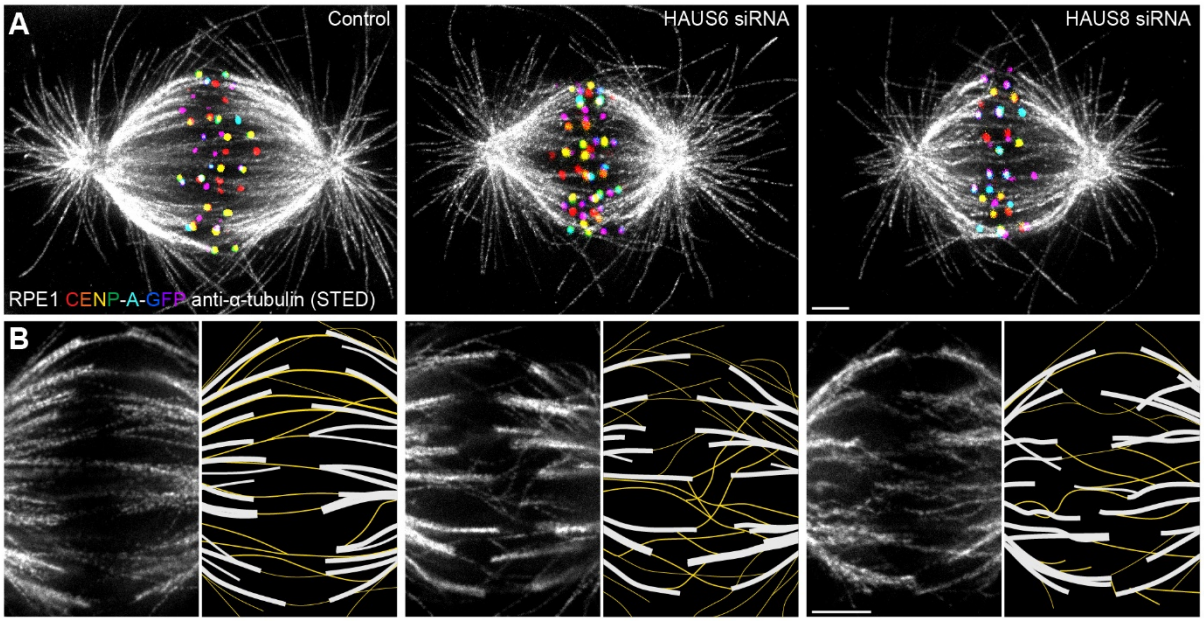


**Figure 1. Augmin ensures the proper formation of entities consisting of bridging fibers that connect two sister k-fibers.** (A) STED superresolution images of microtubules immunostained for α-tubulin (gray) in control (left), HAUS6- (middle) and HAUS8-depleted (right) RPE1 cells stably expressing CENP-A-GFP (rainbow, confocal). Images show maximum intensity projections of 6 central z-planes of metaphase spindles. Kinetochores are color-coded for depth from blue to red with the Spectrum LUT in ImageJ. (B) Insets of STED superresolution images of microtubules (gray) in spindle midzones of control (left), HAUS6- (middle) and HAUS8-depleted (right) cells. Next to each image is the schematic representation of the microtubules in the midzone, with white lines representing k-fiber microtubules and yellow lines representing midplane-crossing microtubules. Images show a single z-plane and do not correspond to midzones of spindles in panel (A). All images are adjusted for clarity based on the intensity of astral microtubules in each image. Scale bars, 2 µm.

## Augmin helps both prevent and resolve segregation errors through joint action of bridging and k-fibers

The appearance of disordered midplane-crossing microtubules in the metaphase plate area of spindles without augmin prompted us to investigate whether these microtubules affect mitotic fidelity. Augmin depletion has previously been linked to higher incidence of segregation errors (Almeida et al., 2022; Viais et al., 2021; Wu et al., 2008), but their origin remained largely unexplored due to extensive mitotic delays in augmin-depleted cells (Wu et al., 2008). To avoid mitotic delays, we performed live-cell confocal imaging for which we codepleted the checkpoint protein Mad2 together with HAUS6 to induce anaphase onset, and used Mad2-

depleted cells (Mayr et al., 2007), which have only a few segregation errors, as a control (Fig. 2A, Supplementary Video 1 and 2). To explore the mechanistic origin of segregation errors, we divided them into three distinct groups: misaligned chromosomes in which both kinetochores were found outside the metaphase plate just before anaphase onset, lagging chromosomes in which the kinetochore is visibly stretched and positioned in the central part of the spindle while other kinetochores are already separating, and other less common and diverse errors (Fig. 2A-B, See Methods).

The treatment with Mad2 siRNA resulted in a total of 1.5 ± 0.2 segregation errors per cell (all data are given as mean ± SEM). However, the effect was significantly more severe when Mad2 was codepleted with HAUS6, resulting in a total of 5.7 ± 0.8 segregation errors per cell (Fig. 2B). Tracking of sister kinetochores in live-cell videos revealed that the number of misaligned kinetochore pairs per cell was similar in both Mad2 depletion and Mad2/HAUS6 codepletion (Fig 2B), which is why we presume they appeared due to Mad2 depletion independently of HAUS6 depletion. Nevertheless, they were much more likely to missegregate in cells without HAUS6, where 80 ± 9% of kinetochore pairs jointly segregated into the same cell, compared to only 20 ± 13% in control cells (Fig. 2B). Interestingly, lagging kinetochores were both more frequent and more likely to missegregate in cells with Mad2/HAUS6 codepletion, in which there were 2.6 ± 0.4 lagging kinetochores per cell, and 45 ± 6% of all lagging kinetochores ultimately missegregated. In contrast, there were only 0.8 ± 0.2 lagging kinetochore pairs per cell in Mad2 depletion, and 77 ± 8% of them segregated correctly (Fig. 2B). Finally, errors classified as others were more frequent in cells with Mad2/HAUS6 codepletion when compared to those with Mad2 depletion, but not more prone to missegregation (Fig. 2B).

As misaligned chromosomes appeared equally frequently in Mad2 depletion and Mad2/HAUS6 codepletion, but differed in their ability to correctly segregate, we used them as a tool to isolate the role of augmin in resolving segregation errors during anaphase. Consistent with previous findings (Uehara et al., 2009), both poleward movement of kinetochores during anaphase A and spindle elongation during anaphase B were reduced following Mad2/HAUS6 codepletion (Supplementary Fig. S2D-F). To analyze in detail the movement of misaligned kinetochore pairs, we tracked both kinetochores with respect to the proximal and distal pole, i.e. the pole which is closer to the misaligned kinetochore pair or the pole which is further away from it, respectively. The kinetochore closer to the proximal pole approached the proximal pole during anaphase A both after Mad2 depletion and Mad2/HAUS6 codepletion, thereby moving towards the pole to which it should segregate in both cases (Fig. 2C). However, the kinetochore further

away from the proximal pole usually remained stagnant for a short period of time, and afterwards typically moved towards the distal pole and accurately segregating as a "lazy" kinetochore (Sen et al., 2021) in Mad2-depleted cells. In contrast, the kinetochore further away from the proximal pole experienced a short stagnation period and then typically moved away from the pole to which it should segregate, thereby missegregating in Mad2/HAUS6-codepleted cells (Fig 2D, Supplementary Fig. S2G-H). As the interkinetochore distance of both correctly and incorrectly segregating misaligned kinetochore pairs in Mad2/HAUS6-codepleted cells was similar (Fig. 2E), the absence of biorientation is unlikely to be the cause of missegregation for these kinetochores. Instead, missegregation likely occurs due to k-fibers with fewer microtubules (Almeida et al., 2022; Uehara et al., 2009; Zhu et al., 2008), creating insufficient force to move the kinetochore towards the distal pole (Dudka et al., 2018), against the movement of neighboring kinetochores and the corresponding chromosome mass which travel towards the proximal pole (Fig. 2A, Supplementary Video 2).

Whereas lagging chromosomes have been previously observed following augmin depletion (Almeida et al., 2022; Viais et al., 2021; Wu et al., 2008), their origin remains unknown. Because we observed that disorganized midplane-crossing microtubules were often concentrated in the inner part of the mitotic spindle near the main spindle axis upon augmin depletion (Fig. 1B, Supplementary Fig. S1), we decided to investigate the spatial distribution (Fig. 2F) of lagging kinetochores in Mad2-depleted and Mad2/HAUS6-codepleted cells to see if their increased number might be connected to this phenotype. In Mad2-depleted cells, all lagging kinetochore pairs were situated in the outer half of the spindle just before anaphase onset. Remarkably, in Mad2/HAUS6-codepleted cells, 19 ± 5% of all lagging kinetochore pairs were situated in the inner part of the spindle just before anaphase onset (Fig. 2F), where disordered midplane-crossing microtubules most frequently appeared. Thus, organization of midplane-crossing microtubules into bridging fibers might play an important role in mitotic fidelity.

To further explore how this compromised spindle geometry affects lagging kinetochores, we measured their interkinetochore distance just before anaphase onset. The lagging kinetochore pairs in Mad2/HAUS6-codepleted cells had an interkinetochore distance of 0.89 ± 0.03 µm, which was significantly smaller than the interkinetochore distance of 0.98 ± 0.02 µm measured in error-free kinetochore pairs (Fig. 2G). This was not the case for lagging kinetochore pairs in Mad2-depleted cells which had an interkinetochore distance of 1.10 ± 0.05 µm, similar to the interkinetochore distance of 1.05 ± 0.02 µm measured in error-free kinetochore pairs (Fig. 2G).

Distinctly reduced interkinetochore distance of lagging kinetochore pairs following Mad2/HAUS6 codepletion suggests that they appear due to compromised spindle architecture being unable to maintain adequate kinetochore tension.

As sister k-fibers in the disorganized spindle region were sometimes diagonally positioned with respect to the pole-to-pole axis, we decided to test if this tilt is also connected to the appearance of segregation errors by measuring the angle that either lagging or error-free kinetochores form with the spindle axis just before anaphase onset. As for the interkinetochore distance following Mad2/HAUS6 codepletion, lagging kinetochore pairs were different from error-free kinetochore pairs, the tilt of which was 19.7 ± 1.6˚ and 10.9 ± 0.8˚, respectively (Fig. 2H). In contrast, in Mad2-depleted cells with preserved spindle geometry there was no difference between lagging kinetochore pairs with the tilt of 8.2 ± 1.5˚ and error-free kinetochore pairs with the tilt of 8.9 ± 0.6˚, which was also similar to the tilt of 10.9 ± 0.8˚ measured for error-free kinetochore pairs following Mad2/HAUS6 codepletion (Fig 2H). The tilt of kinetochores inversely correlated with the interkinetochore distance in augmin depletion, but not in control cells (Fig. 2I). These data indicate the importance of nearly parallel configuration of kinetochore pairs during metaphase for mitotic fidelity, and points to the augmin-specific cause of lagging kinetochores that likely arise due to compromised and tilted bundle architecture facilitating the formation of merotelic attachments. Indeed, we found merotelic attachments in HAUS6-depleted cells imaged using STED microscopy, with most kinetochores forming an attachment with the microtubule from the opposite side of the mitotic spindle, while missing a proper bridging fiber (Fig. 2J). To further test the nature of the observed attachments, we combined STED microscopy with cold treatment to remove midplane-crossing microtubules and preserve only kinetochore microtubules (DeLuca et al., 2006; Sacristan et al., 2018; Silkworth et al., 2011), which allowed us to confirm their true merotelic nature (Fig. 2K). Interestingly, our live-cell imaging experiments reveal that augmin is required not only to prevent the formation of merotelic attachments in metaphase, but also to resolve them in anaphase, as a larger percentage of lagging kinetochore pairs ends up missegregating in Mad2/HAUS6 codepletion than in Mad2 depletion (Fig. 2B). This suggests that the insufficient force provided by k-fibers with fewer microtubules (Dudka et al., 2018), which is responsible for missegregation of misaligned kinetochore pairs following augmin depletion, also leads to inability to resolve merotelic attachments during anaphase.

Altogether, we propose that augmin ensures mitotic fidelity through the joint action of bridging and k-fibers. While augmin-nucleated bridging fibers prevent merotelic attachments by creating

a nearly parallel and highly bundled spindle geometry unfavorable for creating additional attachments, augmin-nucleated k-fibers produce robust force required to resolve any potentially appearing errors during anaphase (Fig. 2L).

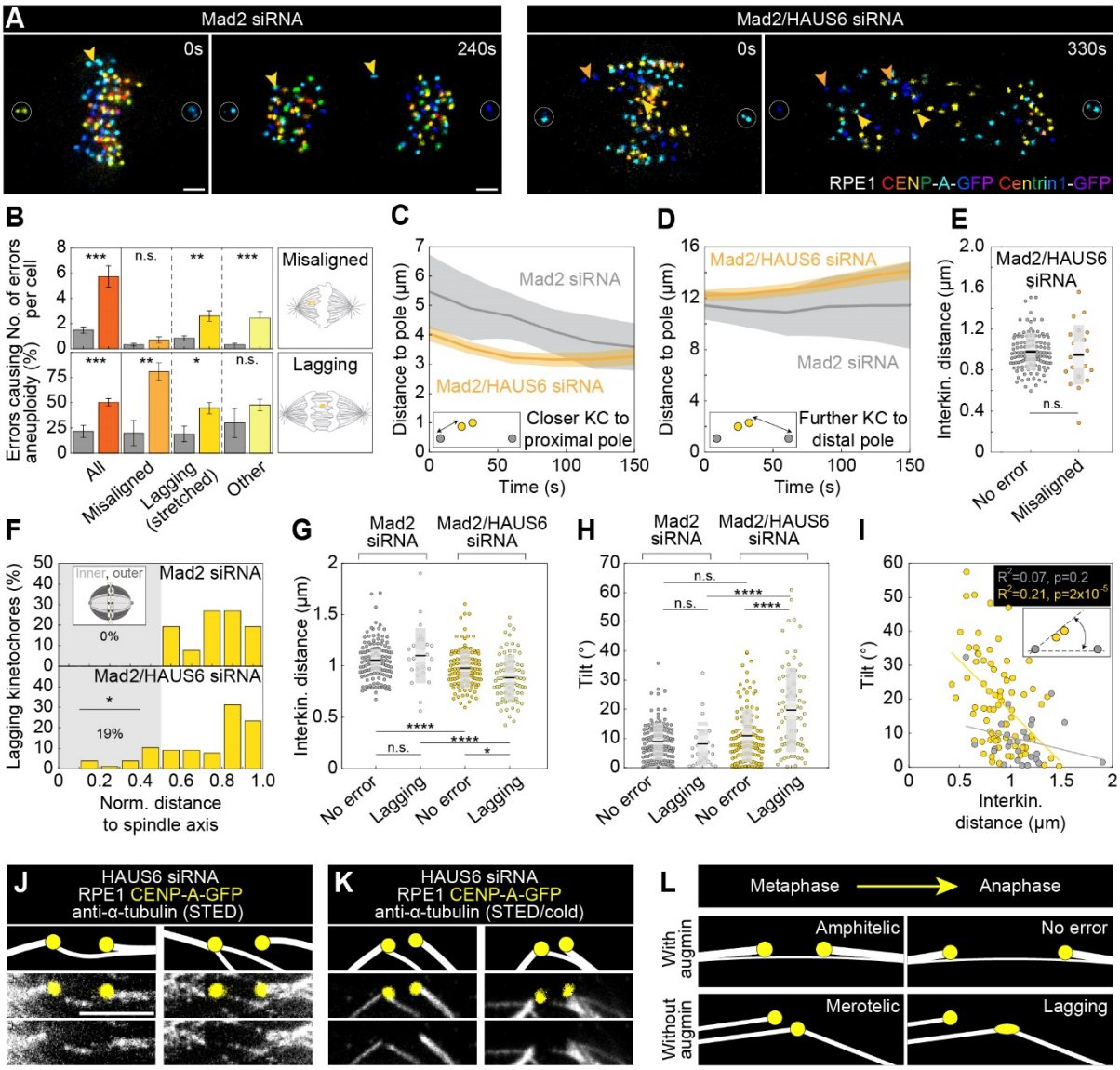


**Figure 2. Augmin-nucleated midplane-crossing microtubules work together with kinetochore microtubules to promote mitotic fidelity.** (A) Time-lapse images of RPE1 cells stably expressing CENP-A-GFP and Centrin1-GFP (rainbow, confocal) in Mad2-depleted cells (left) and Mad2/HAUS6-codepleted cells (right). Yellow arrows represent lagging kinetochores and orange arrows misaligned kinetochores. Kinetochores are color-coded for depth from blue to red with the 16 Colors LUT in ImageJ. (B) The number of segregation errors per cell (top) and the percentage of errors causing aneuploidy (bottom) in Mad2-depleted cells (gray) and Mad2/HAUS6-codepleted cells (dark orange, light orange, dark yellow, light yellow). All segregation errors (dark orange) are divided into three groups: misaligned (light orange), lagging (dark yellow) and other (light yellow). Schematic representations right to the graph represent misaligned kinetochores (top) and lagging kinetochore (bottom). The number of errors in Mad2-depleted cells - in total 46 errors in 22 out of 31 cells; 10 misaligned kinetochore pairs in 9 out of 31

cells; 26 lagging kinetochores in 16 out of 31 cells; 10 other errors in 9 out of 31 cells. Number of errors in Mad2/HAUS6-codepleted cells - in total 172 errors in 25 out of 30 cells; 21 misaligned kinetochore pairs in 11 out of 30 cells; 78 lagging kinetochores in 23 out of 30 cells; 73 other errors in 20 out of 30 cells. Aneuploidy in Mad2-depleted cells - in total 11/46 errors in 22 out of 31 cells; 2/10 misaligned kinetochore pairs in 9 out of 31 cells; 6/26 lagging kinetochores in 16 out of 31 cells; 3/10 other errors in 9 out of 31 cells. Aneuploidy in Mad2/HAUS6-codepleted cells - in total 47/172 errors in 25 out of 30 cells; 17/21 misaligned kinetochore pairs in 11 out of 30 cells; 35/78 lagging kinetochores in 23 out of 30 cells; 35/73 other errors in 20 out of 30 cells. (C) The distance of closer kinetochore to the proximal pole and (D) further kinetochore to the distal pole of misaligned kinetochore pairs in time for Mad2-depleted (gray) and Mad2/HAUS6-codepleted cells (orange). Values are shown as mean (dark line) and SEM (shaded areas). The insets show the positions of kinetochores (yellow) with respect to spindle poles (gray). (E) Univariate scatter plot of the interkinetochore distance of error-free kinetochore pairs (gray) and misaligned kinetochore pairs (orange) in Mad2/HAUS6-codepleted cells. N = 30 cells and 120 error-free kinetochore pairs in Mad2-depleted cells and N = 30 cells and 21 misaligned kinetochore pairs in Mad2/HAUS6-codepleted cells. (F) The percentage of lagging kinetochores in Mad2-depleted (top) and Mad2/HAUS6-codepleted cells (bottom) divided by their location with respect to the pole-to-pole axis to inner and outer (schematic representation shown as inset, see Methods). (G) Univariate scatter plot of the interkinetochore distance of error-free and lagging kinetochore pairs in Mad2-depleted (gray) and Mad2/HAUS6-codepleted cells (yellow). (H) Univariate scatter plot of the angle that the error-free and lagging kinetochore pairs form with the pole-to-pole axis (tilt) in Mad2-depleted (gray) and Mad2/HAUS6-codepleted cells (yellow). N = 31 cells and 124 error-free and 26 lagging kinetochore pairs from Mad2-depleted cells. N = 30 cells and 120 error-free and 78 lagging kinetochore pairs from Mad2/HAUS6-codepleted cells. (I) The correlation of the tilt and the interkinetochore distance for Mad2-depleted (gray) and Mad2/HAUS6-codepleted cells (yellow). Inset shows schematic representation of the tilt (kinetochores are shown in yellow and spindle poles in gray). (J) The insets of kinetochore pairs with merotelic attachments in RPE1 cells stably expressing CENP-A-GFP (yellow, confocal) and immunostained for α-tubulin (gray, STED). (K) The insets of kinetochore pairs from cells as in (J) but exposed to cold treatment. Images in (J) and (K) are smoothed with 0.5-mm-sigma Gaussian blur. Schematic representations in (J) and (K) are shown above the insets for better visualization of merotelic microtubule attachments. (L) The schematic representations of a kinetochore pair with amphitelic attachment in metaphase that does not cause any segregation errors during anaphase when augmin is present (top) and a kinetochore pair with merotelic attachment in metaphase that ends up as the lagging kinetochore during anaphase when augmin is not present (bottom). (E, G and H) Boxes represent standard deviation (dark gray), 95% confidence interval of the mean (light gray) and mean value (black). All results were obtained from three independent experiments. Statistical analysis (B (top) and E) Mann–Whitney U test; (B (bottom) and F) Fisher's exact test; (G and H) ANOVA with the post-hoc Tukey test; (I) linear regression; p-value legend: < 0.0001 (****), 0.0001 to 0.001 (***), 0.001 to 0.01 (**), 0.01 to 0.05 (*), ≥ 0.05 (ns). Scale bars, 2 μm.

## Bridging fibers are predominantly generated through augmin-dependent nucleation

As our visual assessment revealed that spindles without augmin have disorganized arrangements of midplane-crossing microtubules and often lack proper bridging fibers (Fig. 1B), which were also missing at kinetochore pairs that formed merotelic attachments (Fig. 2J), we set out to analyze how augmin-dependent microtubule nucleation contributes to the formation of bridging fibers in immunostained RPE1 cells imaged using STED microscopy (Fig. 3A-B). Bridging fibers were strictly defined as midplane-crossing microtubules that connect two sister k-fibers, whereas k-fibers were defined as microtubules that start at kinetochores (Fig. 3C). We measured tubulin signal intensity of randomly selected bridging ($I_b$) and k-fibers ($I_k$) which had no other microtubules in their immediate neighborhood, in a small square region between two kinetochores or at the pole-side of kinetochore, respectively (Fig. 3C, see Methods). By using the resulting tubulin signal intensities, we first estimated the number of microtubules in the bridging fiber in untreated RPE1 cells. Electron tomography of spindles in RPE1 cells showed that k-fibers consist of $n_k = 12.6 \pm 1.7$ microtubules (O'Toole et al., 2020). Thus, the bridging fiber consists of $n_b = I_b \times n_k / I_k = 3.8 \pm 0.4$ microtubules (for the explanation of $I_b$ and $I_k$ calculations, see Methods). The accuracy of this calculation was additionally tested by measuring the intensity of astral microtubules, which presumably consist of single microtubules (McDonald et al., 1992). Indeed, using the number of microtubules in the k-fiber, our measurement of astral microtubule intensities showed that the astral microtubules consist of $n_a = 1.0 \pm 0.1$ microtubules (Fig. 3D).

Quantification of STED images further revealed that HAUS6 depletion resulted in 68 ± 8% reduction of the bridging fiber signal intensity and 24 ± 6% reduction of the k-fiber signal intensity, with similar results obtained by HAUS8 depletion (Fig. 3D-E). These data indicate that augmin depletion affects not only k-fibers, but even more so bridging fibers. The contribution of augmin to the nucleation of k-fibers was independently tested by measuring their intensity in spindles exposed to cold treatment in which bridging fibers are removed (Fig. 3F). HAUS6 depletion resulted in a 37 ± 5% reduction of the k-fibers (Fig. 3G), which is consistent with a previous study (Zhu et al., 2008) and comparable to values under non-cold conditions. Based on the measurements under non-cold conditions, we estimate that after HAUS6 depletion bridging fibers consist of 1.2 ± 0.7 microtubules and k-fibers of 9.6 ± 1.5 microtubules, which we interpret as microtubules nucleated in an augmin-independent manner. Thus, 2.6 ± 0.7 microtubules in the bridging fiber and 3.0 ± 0.9 microtubules in the k-fiber are nucleated in an augmin-dependent manner.

Remarkably, 41 ± 4% of all kinetochore pairs in HAUS6-depleted cells had no detectable bridging fibers, defined as those with the tubulin signal below the background signal (see Methods), and consistent with results obtained using visual inspection (Supplementary Fig. S3A). The majority of kinetochore pairs without bridging fibers were located in the inner part of the mitotic spindle, where as much as 50 ± 5% of all kinetochore pairs had undetectable bridging fibers after augmin depletion, compared to only 27 ± 5% percent in the outer part (Fig. 3H), thus pointing to an irregular and more complex spatial distribution of bridging fibers in the inner part of the spindles following augmin depletion. Similar results were obtained from superresolution imaging after HAUS8 depletion (Fig. 3H). To further validate our results, we performed live-cell confocal imaging with SiR-tubulin (Lukinavičius et al., 2014) and analyzed the spindles by two independent methods (Supplementary Fig. S3A-H, See Methods). Altogether, these results reveal that the augmin complex is a major nucleator of bridging fibers, whereas its contribution to the formation of k-fibers is significant but less prominent.

The compromised microtubule nucleation following augmin depletion led to the impairment of overall spindle geometry, creating a unique system where three main types of interactions between k-fibers and bridging fibers can be found within the same spindle: (1) sister k-fibers attached to bridging fibers, (2) sister k-fibers without a bridging fiber, and (3) solitary, long, interpolar bundles without associated kinetochores. This is in contrast with control cells, where the first group dominates and the other two groups are rarely found (Polak et al., 2017). To gain insight into the contribution of each of these functionally distinct microtubule bundles to the maintenance of spindle geometry, we traced the outermost bundles in HAUS6 siRNA treated RPE1 cells imaged using STED microscopy and fitted a circle to the bundle outline (Supplementary Fig. S3I, see Methods). Whereas the bundles without kinetochores in HAUS6 siRNA-treated cells had a significantly longer contour when compared to all other bundle types (Supplementary Fig. S3J), k-fibers without bridging fibers in augmin-depleted cells had a significantly larger radius of curvature than any of the other bundle types in augmin-depleted or control cells (Supplementary Fig. S3K). Taken together, the outer interpolar bundles without associated kinetochores are excessively long and make the spindle wider, whereas k-fibers lacking a bridging fiber are overly straight, ultimately resulting in a diamond-like shape of the spindle. This change in spindle shape in the absence of proper bridging fibers is consistent with the prediction of our theoretical model (Kajtez et al., 2016) and previous experiments (Jagrić et al., 2021).

In addition to spindle architecture, compromised microtubule nucleation following augmin depletion also affected spindle dynamics, as poleward flux in U2OS cells stably expressing CENP-A-GFP, mCherry-tubulin and photoactivatable-GFP-α-tubulin was significantly reduced (Supplementary Fig. S3L-M), in agreement with findings in Indian Muntjac cells (Almeida et al., 2022). Recent speckle microscopy experiments in RPE1 cells, which were able to separate the effect of augmin on poleward flux of bridging and k-fibers, revealed that both k-fibers and the remaining bridging fibers were significantly slowed down (Risteski et al., 2021 *Preprint*). Bridging fibers fluxed faster than k-fibers in control and augmin-depleted cells (Risteski et al., 2021 *Preprint*), supporting the model in which poleward flux is largely driven by sliding apart of antiparallel microtubules (Brust-Mascher et al., 2009; Mitchison, 2005; Miyamoto et al., 2004). We propose that augmin depletion results in slower flux of bridging fibers because the remaining bridging microtubules are likely nucleated at the poles, where microtubule depolymerization mechanisms might curb poleward flux speed (Ganem et al., 2005). In contrast, PRC1 depletion does not affect the flux (Risteski et al., 2021 *Preprint*; Steblyanko et al., 2020) even though it reduces bridging fibers (Kajtez et al., 2016; Polak et al., 2017), possibly because the remaining bridging microtubules are generated away from the poles via augmin and can thus flux freely. In sum, augmin ensures proper architecture and dynamics of the metaphase spindle largely through the nucleation of bridging fibers, which link sister k-fibers and ensure their proper shape and function.

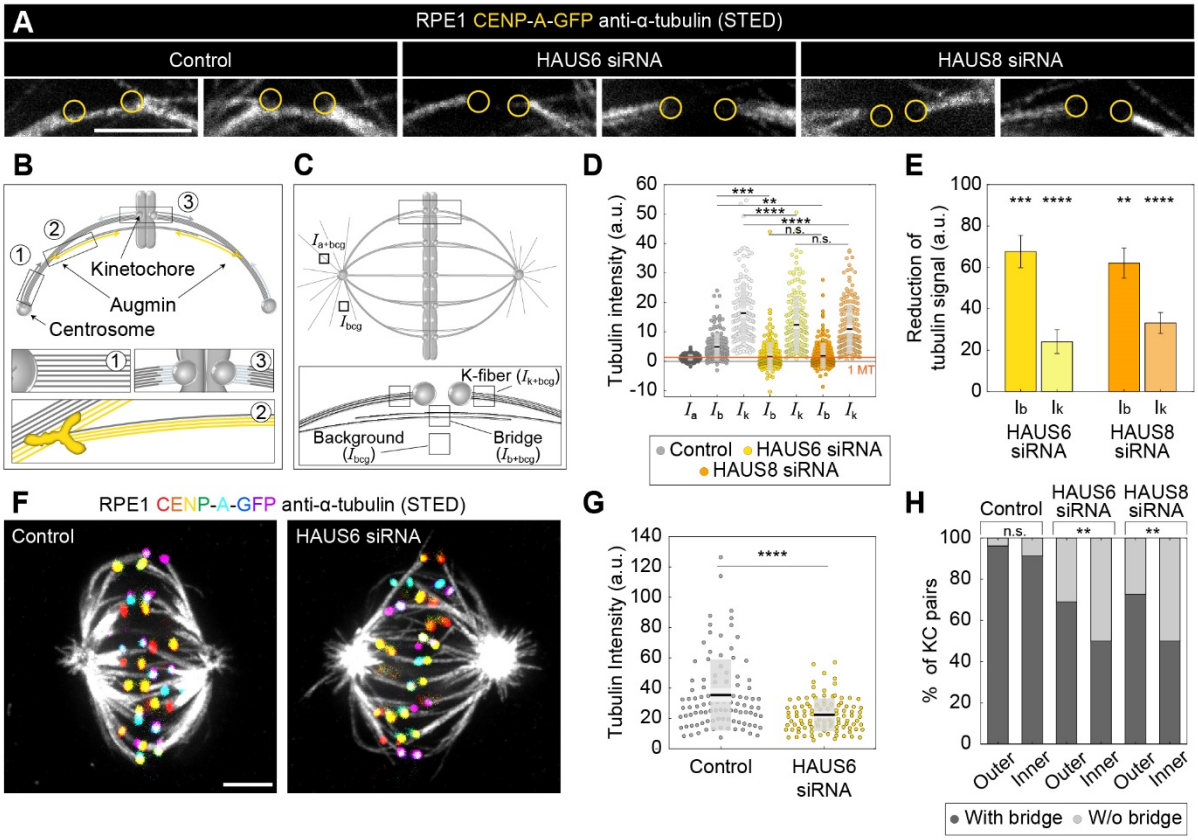


**Figure 3. Augmin is crucial for the nucleation of bridging microtubules.** (A) The insets of kinetochore pairs in RPE1 cells stably expressing CENP-A-GFP (not shown) immunostained for α-tubulin (gray, STED) in control cells (left) and after HAUS6 (middle) or HAUS8 (right) depletion. The insets demonstrate kinetochore pairs with bridging fibers affected by HAUS6 or HAUS8 depletion compared to bridging fibers in control cells. The positions of kinetochores are marked with yellow circles. (B) The schematic representation of three possible pathways of microtubule nucleation: 1) centrosome-dependent 2) augmin-dependent and 3) chromatin- and kinetochore-dependent nucleation. The augmin complex is shown in yellow. (C) Top: the schematic representation of the mitotic spindle in metaphase and the method used to measure the tubulin intensity of the astral microtubules. Small square regions were measured on microtubules extending from the spindle pole, corresponding to astral microtubules. Their background was measured in the empty area between the two astral microtubules, and it was subtracted from astral microtubule intensity. Bottom: Schematic representation of the method used to measure the tubulin intensity of the bridging and k-fiber. Small square regions were measured between two kinetochores or right next to the kinetochore, corresponding to bridging and k-fibers, respectively. The intensity of k-fibers was measured as an average of two sister k-fibers, and the average value of the background within the spindle was subtracted from all measurements. $I_{a+bcg}$ = intensity of astral microtubules with background, $I_{k+bcg}$ = intensity of k-fibers with background, $I_{b+bcg}$ = intensity of bridging microtubules with background, $I_{bcg}$ = intensity of background. (D) Univariate scatter plot of tubulin signal intensities of astral microtubules in control cells (reference value, dark gray, $I_a$), and bridging fibers ($I_b$) and k-fibers ($I_k$) in control cells (gray), HAUS6- (yellow) and HAUS8-depleted cells (orange). (E) The reduction of tubulin signal in the bridging fiber ($I_b$) and the k-fiber ($I_k$) following HAUS6 (yellow) or HAUS8 (orange) depletion, values are shown as mean ± SEM. P-values were calculated using the absolute values of tubulin signal intensity of bridging or k-fibers following HAUS6 or HAUS8

depletion, compared to the absolute values of tubulin signal intensity of corresponding fibers in control cells. (D) and (E) N = 30 cells and 90 astral microtubules in control cells, 158 bridging and sister k-fibers in control and 180 bridging and sister k-fibers in HAUS6- and HAUS8 siRNA-treated cells. (F) STED superresolution images of microtubules stained for α-tubulin (gray) in RPE1 cells stably expressing CENP-A-GFP (rainbow, confocal) in control cells (left) and HAUS6 siRNA-treated cells (right) exposed to cold treatment. The images are maximum intensity projections and kinetochores are color-coded for depth from blue to red with the Spectrum LUT in ImageJ. (G) Univariate scatter plot of the tubulin signal intensities of k-fibers in control cells (gray) and upon HAUS6 depletion (yellow) in cells exposed to cold treatment. N = 30 cells and 101 bundles in control cells and 102 bundles in HAUS6-depleted cells. (H) The fractions of kinetochore pairs with bridging fibers (dark gray) and with undetectable bridging fibers (light gray) in control, HAUS6- and HAUS8-depleted cells. Kinetochore pairs are divided based on their location in the spindle to outer and inner (See Methods and Results). (D) and (G) Boxes represent standard deviation (dark gray), 95% confidence interval of the mean (light gray) and mean value (black). All results were obtained from three independent experiments. Statistical analysis (D and E) ANOVA with post-hoc Tukey test, (G) Mann–Whitney U test, (H) chi-square test; p-value legend: < 0.0001 (****), 0.0001 to 0.001 (***), 0.001 to 0.01 (**), 0.01 to 0.05 (*), ≥ 0.05 (ns). All images are adjusted for clarity. Scale bars, 2 µm.

## Augmin-depleted spindles contain fewer overlap bundles, which have longer overlap regions and are located at the spindle periphery

Our finding that bridging fibers were more severely perturbed in the inner part of the spindle after augmin depletion prompted us to examine the spatial distribution of these midplane-crossing microtubules and their overlap regions throughout the spindle. We used protein regulator of cytokinesis 1 (PRC1) as a marker because it preferentially crosslinks overlap microtubules (Li et al., 2018; Mollinari et al., 2002), thus providing a specific label for bridging fibers (Polak et al., 2017). By taking a standard "side view" of the spindle and rotating the 3D image stack of the spindle into an "end-on" view, we were able to gain insight into the redistribution of bridging microtubules throughout the spindle cross-section in HeLa (Kajtez et al., 2016) and RPE1 (Asthana et al., 2021) cells stably expressing PRC1-GFP with and without MG-132 treatment (Fig. 4A-B, Supplementary Fig. S4A). To compare their distribution to that of tubulin, we also rotated the 3D image stacks of the spindles in RPE1 cells stained with SiR-tubulin (Fig.4A-B, Supplementary Fig. S4B) (Novak et al., 2018).

The signal intensity of PRC1-GFP bundles in RPE1 cells was reduced by 55 ± 4% following augmin depletion (Fig. 4C). Consistently, the number of PRC1-labeled overlap bundles measured in an end-on view of spindles was almost halved; from 28 ± 1 to 16 ± 1 distinct bundles in control and HAUS6-depleted RPE1 cells, respectively (Fig. 4D). Comparable trends

were also observed in HeLa cells after depletion of HAUS6 or HAUS8 (Supplementary Fig S4C-G).

The augmin-depleted cells showed a specific barrel-like distribution of the PRC1-GFP labeled bundles, with more overlap bundles being present around the perimeter of the spindle and fewer in the central part (Fig. 4A "end-on view" and 4D, Supplementary Fig. S4H-I). However, DNA was uniformly distributed throughout the spindle cross-section, both in augmin-depleted and control cells (Fig. 4A "end-on view"). In agreement with this result, kinetochores and tubulin signal were also found uniformly distributed over the spindle cross-section (Fig. 4A “end-on view” of RPE1 cells). This observation indicates that k-fibers are present and roughly uniformly distributed throughout the spindle cross-section and is in agreement with our finding that augmin primarily affects bridging fibers, while k-fibers are less perturbed (Fig. 3).

To explore the role of the observed overlap repositioning in defining the overall spindle geometry, we measured spindle width, the diameter of the metaphase plate, spindle length, and overlap length in RPE1 and HeLa cells (see Methods). Despite the spindles being wider in both cell lines, the diameter of the metaphase plate was not larger, as the spindles widened due to the long, curved bundles without kinetochores (Supplementary Fig. S4J). While the spindles in RPE1 cells shortened following augmin depletion, those in HeLa cells were longer (Supplementary Fig. S4J), consistent with previous observations on *Drosophila* S2 cells and *Xenopus* egg extracts (Goshima et al., 2007; Petry et al., 2011). This difference in spindle length might be due to the overlaps remaining the same length after augmin depletion in RPE1 cells, while being longer and thereby able to push the spindle poles further apart in HeLa cells (Supplementary Fig. S4K). When both spindle length and overlap length were taken into account, the relative length of overlaps with respect to spindle length increased in RPE1 cells from 48 ± 1% to 57 ± 2% following augmin depletion (Fig. 4F), comparable to the increase in HeLa cells (Supplementary Fig. S4L-M). Altogether, these results suggest that augmin regulates both the width and length of metaphase spindles, while also restricting the portion of spindle length occupied by overlap microtubules.

Interestingly, the long curved bundles characteristic for augmin depletion (Goshima et al., 2008; Uehara et al., 2016; Wu et al., 2008; Zhu et al., 2008) exhibited PRC1 signal along most of their length, suggesting that they consist of antiparallel microtubules, even though contrary to bridging fibers, they form away from the k-fibers and kinetochores (corresponding to long, curved bundles in Fig. 1A and Supplementary Fig. S3I). These bundles likely arose either due to PRC1 crosslinking excessively long astral microtubules that were now able to reach the

spindle midzone or due to PRC1 activity combined with the excess of free tubulin present as a consequence of less tubulin being incorporated in bridging and k-fibers. Altogether, the data suggest that there was an overall redistribution of PRC1 within the spindle from a large number of relatively short overlaps to a small number of relatively long overlaps. These results were further corroborated by PRC1-antibody staining in unlabeled HeLa cells, which also showed a reduced number of elongated PRC1 signals along the curved outer bundles after augmin depletion (Supplementary Fig. S4F). Thus, without augmin, the spindles are wider and contain fewer overlaps, which occupy a larger portion of spindle length and tend to accumulate at the spindle periphery.

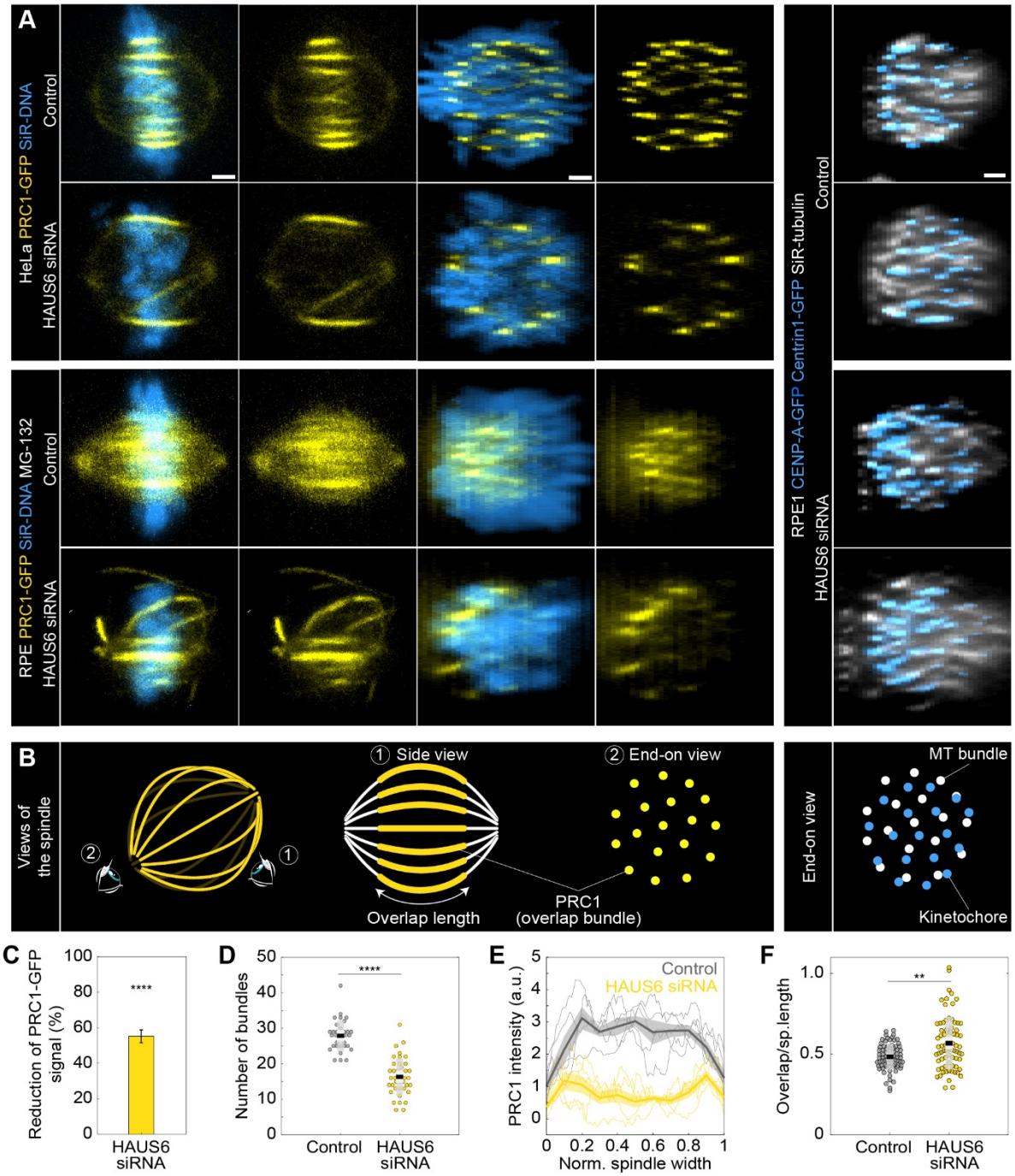


**Figure 4. In augmin-depleted spindles the number of bridging fibers decreases, with the remaining ones having an increased overlap length and being located at the spindle periphery.** (A) The four columns on the left represent live images of metaphase spindles in untreated HeLa or MG-132 treated RPE1 cells stably expressing PRC1-GFP (yellow) and stained with SiR-DNA (blue) in control cells (top rows) and after HAUS6 depletion (bottom rows). 1st and 2nd column: side view of the spindle; 3rd and 4th column: end-on view of the same spindle, showing a barrel-like arrangement of PRC1-labeled bundles after augmin depletion. Images on the right show the end-on view of RPE1 cells stably expressing CENP-A-GFP and Centrin1-GFP (both in blue) and stained with SiR-tubulin (gray) in control cells (top) and after HAUS6 depletion (bottom). Side views are sum intensity projections of 5 central z-slices (Δz=0.5 µm) in HeLa cells and 10 central z-slices for RPE1 cells. End-on views

are sum projections of 10 central z-slices (Δz=0.083 µm) for HeLa and 20 central z-slices for RPE1 cells. (B) Left: schematic representations of different views of the spindle. Eye signs mark the angle for the side view (1) and the end-on view (2). Side view was used to measure the length of overlap regions (yellow) and end-on view to determine the number of bundles (yellow dots). Right: schematic representation of the end-on view of RPE1 cells stably expressing CENP-A-GFP and Centrin1-GFP (blue dots) and stained with SiR-tubulin (gray dots). (C) The reduction of the PRC1 signal in RPE1 cells treated with MG-132 measured in sum intensity projection of 10 central z-slices following HAUS6 depletion. Values are shown as mean ± SEM. P-values were calculated using the absolute values of PRC1 signal intensity following HAUS6 depletion (N = 39 cells), compared to the absolute values of PRC1 signal intensity in control cells (N = 32 cells). (D) Univariate scatter plot of the number of bundles in RPE1 cells treated with MG-132 counted in the end-on view of the spindle in control cells (gray) and HAUS6-depleted cells (yellow). N = 32 control cells and N = 39 HAUS6-depleted cells. (E) The PRC1-GFP intensity profiles in RPE1 cells treated with MG-132 measured in the end-on view of the spindle in control cells (gray) and after HAUS6 depletion (yellow). The blue line in the inset marks the measured region (width: 2.5 µm). Mean (thick lines) and SEM (shaded areas). (F) Univariate scatter plot of overlap length divided by spindle length in RPE1 cells treated with MG-132 measured in the side view of the spindle in control cells (gray) and HAUS6-depleted cells (yellow). N = 75 bundles in 32 control cells and N = 74 bundles from 39 HAUS6-depleted cells. (D and F) Boxes represent standard deviation (dark gray), 95% confidence interval of the mean (light gray) and mean value (black). All results were obtained from three independent experiments. Statistical analysis (C, D and F) Mann–Whitney U test; p-value legend: < 0.0001 (****), 0.0001 to 0.001 (***), 0.001 to 0.01 (**), 0.01 to 0.05 (*), ≥ 0.05 (ns). All images are adjusted for clarity. Scale bars, 2 µm.

## The interkinetochore distance decreases preferentially in the inner part of the spindle and at kinetochores with weaker bridging fibers after augmin depletion

The interkinetochore distance, which is a readout of interkinetochore tension (Waters et al., 1996), decreases after augmin depletion (Uehara et al., 2009; Zhu et al., 2008). Our measurements on RPE1 and HeLa cells also showed a reduced interkinetochore distance in augmin-depleted cells (Supplementary Fig. S5A). This reduction of interkinetochore tension may be due to weaker k-fibers (Uehara et al., 2009; Zhu et al., 2008). However, we noticed that the interkinetochore distance was smaller in the inner part of the spindle in augmin-depleted cells (Fig. 5A-D, Supplementary Fig. S5B), where bridging fibers were most severely impaired (Fig. 3H and 4A). This was not the case in control cells, which showed no difference in interkinetochore distance between the inner and the outer part of the spindle (Fig. 5D, Supplementary Fig. S5B). These findings motivated us to investigate a potential link between the lack of proper bridging fibers and the interkinetochore tension. We thus divided kinetochore pairs in STED images into two groups: (1) those with a bridging fiber (i.e., signal intensity of the bridging fiber above the background signal), and (2) those with undetectable signal

intensities at the expected locations of bridging fibers, which we for simplicity refer to as kinetochore pairs without bridging fibers (Fig. 5B-C). Remarkably, kinetochore pairs without bridging fibers had a significantly smaller interkinetochore distance than kinetochore pairs with bridging fibers (Fig. 5E).

Though this result suggests a role of bridging fibers in regulating interkinetochore distance, this effect may be indirect and arise due to k-fibers because kinetochore pairs that lacked a bridging fiber typically had thinner k-fibers than those with a bridging fiber in augmin-depleted cells (Supplementary Fig. S5C). Hence, we used several approaches to separate the contribution of bridging and k-fibers to the interkinetochore tension. First, we found that although the interkinetochore distance correlated both with bridging and k-fiber intensity after augmin depletion, the correlation with bridging fiber intensity was stronger (Supplementary Fig. S5D-E). Such correlations were absent in control cells (Supplementary Fig. S5D-E). To explore a specific contribution of k-fibers to the interkinetochore tension, we divided the kinetochore pairs in augmin-depleted cells into two subsets, those with and without bridging fibers, and found that the interkinetochore distance did not correlate with k-fiber intensity within each group (Fig. 5F), which argues against the k-fiber intensity as a sole determinant of interkinetochore tension. In agreement with this, when we selected two subsets of kinetochore pairs with either very strong or very weak k-fiber intensity but with comparable bridging fiber intensities (Supplementary Fig. S5F-G), we found no difference in the interkinetochore distance between these subsets (Supplementary Fig. S5H). Finally, to examine a specific contribution of bridging fibers, we identified two subsets of kinetochore pairs with similar k-fiber intensity values, one of which had bridging fibers and the other which did not (Supplementary Fig. S5I). We found that the interkinetochore distance was larger in the subset with bridging fibers than without (Fig. 5G), indicating a specific effect of bridging fibers on interkinetochore tension. Analysis of live-cell confocal images of RPE1 cells yielded similar results (Supplementary Fig. S5J-M). Based on these data, we conclude that augmin has a significant role in regulating interkinetochore tension through the nucleation of bridging microtubules.

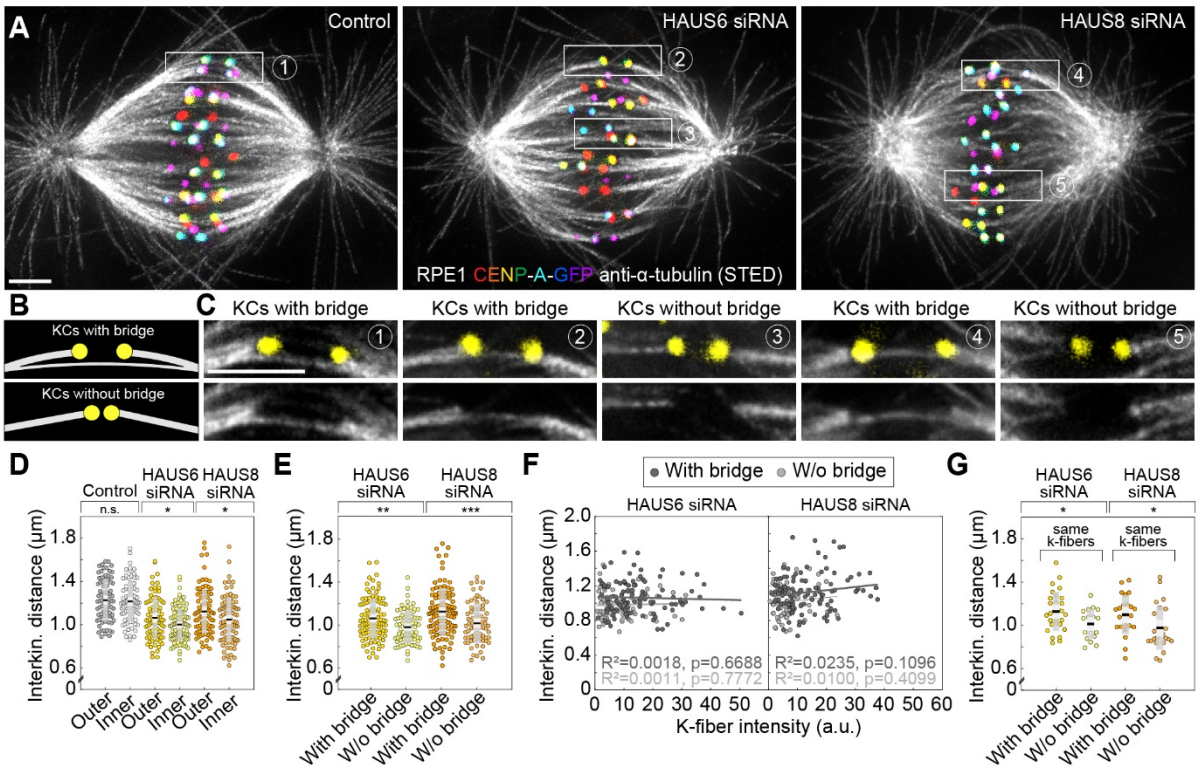


**Figure 5. The reduction of the interkinetochore distance after augmin depletion is related to the impairment of bridging fibers.** (A) STED superresolution images of microtubules immunostained for α-tubulin (gray) in control (left), HAUS6- (middle) and HAUS-8 depleted (right) RPE1 cells stably expressing CENP-A-GFP (rainbow, confocal). Images are maximum intensity projections and kinetochores are color-coded for depth from blue to red with the Spectrum LUT in ImageJ. (B) The schematic representation of a kinetochore pair (KCs) with (top) and without (bottom) bridging fiber (See Results). (C) Enlarged boxes show KCs with or without a bridging fiber in control (left), HAUS6- (middle) and HAUS8- (right) depleted RPE1 cells. Images represent single z-plane taken from spindles in (A) and smoothed with 0.75-mm-sigma Gaussian blur. Kinetochores are shown in yellow. (D) Univariate scatter plot of the interkinetochore distance in control (gray), HAUS6- (yellow) and HAUS8- (orange) depleted cells with kinetochore pairs divided based on their distance from the long (pole-to-pole) spindle axis (outer kinetochore pairs shown in darker colors and inner in lighter colors). N = 30 cells in all three conditions; 78 and 80 outer and inner kinetochore pairs for control, respectively; 84 and 96 outer and inner kinetochore pairs for HAUS6 depletion, respectively; 88 and 92 outer and inner kinetochore pairs for HAUS8 depletion, respectively. (E) Univariate scatter plot of the interkinetochore distance in HAUS6- (yellow) and HAUS8- (orange) depleted cells. Kinetochore pairs are divided into two groups: with bridging fiber (darker colors) and without bridging fiber (lighter colors). N = 30 cells in HAUS6/8-depleted cells; 106 pairs with and 74 kinetochore pairs without bridging fibers in cells following HAUS6 depletion, respectively; 110 and 70 kinetochore pairs with and without bridging fibers in cells following HAUS8 depletion, respectively. (F) The correlation of the interkinetochore distance and the k-fiber intensity for kinetochore pairs with (dark gray) and without (light gray) bridging fiber in HAUS6- (left) and HAUS8-depleted (right) cells. (G) Univariate scatter plot of the interkinetochore distance for HAUS6- (yellow) and HAUS8-depleted (orange) cells. Kinetochore pairs are divided into two groups: with bridging fiber (darker colors) and without bridging fiber (lighter colors), but in this case both

groups have the same k-fiber intensity. N = 27 kinetochore pairs with a bridging fiber and 18 kinetochore pairs without a bridging fiber in HAUS6-depleted cells, respectively; N = 23 kinetochore pairs with and N = 25 kinetochore pairs without a bridging fiber in HAUS8-depleted cells. (D, E and G) Boxes represent standard deviation (dark gray), 95% confidence interval of the mean (light gray) and mean value (black). All results were obtained from three independent experiments. Statistical analysis (D, E and G) t-test for samples that followed normal distribution or Mann–Whitney U test for samples that significantly departured from normality, determined using the Shapiro-Wilk test; (F) linear regression; p-value legend: < 0.0001 (****), 0.0001 to 0.001 (***), 0.001 to 0.01 (**), 0.01 to 0.05 (*), ≥ 0.05 (ns). All images are adjusted for clarity based on the intensity of astral microtubules in each image. Scale bars, 2 µm.

## Discussion

In this paper we propose a model of the metaphase spindle in which the bridging fiber, which laterally connects sister k-fibers, forms by augmin-based nucleation of microtubules along the existing microtubules. The newly nucleated microtubules in the bridging fiber create an antiparallel overlap in which the microtubules slide apart, generating a pushing force that the bridging fiber exerts on its k-fibers. In doing so, the bridging fiber works together with k-fibers to produce tension and maintain the appropriate orientation of sister kinetochores parallel to the spindle axis, thereby preventing merotelic attachments and ensuring mitotic fidelity (Fig. 6).

Our work shows that the depletion of the augmin complex by silencing the HAUS6 or HAUS8 subunits causes severe thinning of bridging fibers in metaphase spindles, combined with the appearance of wavy and disordered midplane-crossing microtubules. Thus, we conclude that the predominant nucleation of bridging microtubules by the augmin complex enables their directional bundling along the sister k-fibers, in agreement with previous observations on directionality of microtubule growth (David et al., 2019; Kamasaki et al., 2013). K-fibers were also thinner, though to a lesser extent, indicating that they are largely nucleated in an augmin-independent manner, at the centrosome or kinetochores and chromosomes. This is in agreement with previous electron microscopy studies of mammalian spindles, where k-fiber microtubules were observed to typically reach the centrosome, while sometimes also extending from the kinetochores with their minus ends within the spindle (Kiewisz et al., 2022 *Preprint*; McDonald et al., 1992; Sikirzhytski et al., 2018), the latter likely representing a combination of microtubules nucleated either at the kinetochores or by the augmin complex. In contrast, most midplane-crossing microtubules, which likely correspond to bridging fibers, start at different points along the k-fiber (Mastronarde et al., 1993). Electron tomography of spindles in RPE1 cells confirmed this result by showing that microtubule minus ends are found along the k-fiber, less than 50 nm from the k-fiber wall and at a distance 2-4 µm from the pole (O'Toole et al., 2020). As we found that the same number of microtubules in bridging and k-fibers was nucleated by augmin, we propose that the existing microtubules orient the growth of augmin-nucleated microtubules (David et al., 2019; Kamasaki et al., 2013), which later become kinetochore microtubules if their plus end binds to the kinetochore or bridging microtubules if they grow past the kinetochore and interact with the bridging or kinetochore microtubules on the other side. However, as there are less microtubules in the bridging fiber to begin with, augmin-mediated nucleation becomes the predominant pathway of their nucleation.

Previous work showed that augmin depletion results in a decrease of interkinetochore distance (Uehara et al., 2009; Zhu et al., 2008), a readout of tension, but it remained unclear if this is due to impaired k-fibers or perturbation of other microtubules. Treatment of cells with a microtubule-destabilizing agent that results in thinner k-fibers causes a reduction of the interkinetochore tension (Dudka et al., 2018), supporting the former possibility. However, a similar effect on the interkinetochore tension was observed upon perturbation of the bridging fiber by removing the microtubule crosslinker PRC1 (Jagrić et al., 2021; Kajtez et al., 2016; Polak et al., 2017), in agreement with the latter possibility. When looking at a subset of kinetochore pairs that had a bridging fiber and those that did not, we found that the tension was more compromised in the latter group. Notably, tension was independent of the k-fiber thickness within each group and depended on the presence or the absence of bridging fibers even when the effect of k-fibers was excluded. Although our experiments cannot directly discern the relative contribution of the bridging and k-fiber impairment in the decrease of tension on kinetochores, they reveal that augmin-generated bridging microtubules have a significant and specific role in the maintenance of interkinetochore tension.

Considering the importance of the interkinetochore tension for the accuracy of cell division (Lampson and Grishchuk, 2017), the maintenance of tension by the bridging fiber might represent an important mechanism for silencing of the spindle assembly checkpoint (Musacchio and Salmon, 2007; Nicklas et al., 1995), supported by the fact augmin-depleted cells with characteristically compromised bridging fibers have extensive mitotic delays (Wu et al., 2008). However, recent work suggests that the reduction of interkinetochore tension caused by k-fiber thinning does not necessarily lead to checkpoint activation, but instead may sometimes result in reduced anaphase A speed caused by low microtubule occupancy, followed by a subsequent increase in lagging chromosomes (Dudka et al., 2018). As proteins involved in bridging fiber nucleation and crosslinking, including HAUS6, HAUS8 and PRC1 have all been linked to various types of cancer (ICGC/TCGA, 2020, retrieved by using cBioPortal (Cerami et al., 2012; Gao et al., 2013)), it is plausible that impairment of bridging fibers also leads to such increase in lagging chromosomes and contributes to aneuploidy. Indeed, once the checkpoint was weakened, lagging chromosomes that appeared following augmin depletion had a reduced interkinetochore distance, which was consistent with previous findings on lazy chromosomes (Sen et al., 2021). However, contrary to previous findings in cells with intact bridging fibers, in which there was no connection between lagging chromosomes and tilt of their kinetochores (Sen et al., 2021), we found that kinetochores of lagging chromosomes in augmin-depleted cells

predominantly form a large tilt with respect to the spindle axis. This suggested that the lack of bridging fibers represents a specific mechanism of predisposing the kinetochore to merotelic attachments by tilting the kinetochores and exposing their surface to the microtubules from the opposite pole. Since the existing kinetochore microtubules no longer orient the growth of midplane-crossing microtubules when augmin is not present, an already tilted kinetochore is also more likely to encounter these microtubules, which puts the kinetochore at an even higher risk of merotelic attachments. Once the merotelic attachments form during metaphase, they might be less likely to undergo error correction in augmin-depleted cells, as bridging fibers might serve as tracks that guide Aurora B within the Chromosome Passenger Complex towards the kinetochores to correct the erroneous attachments (Matković et al., 2022 *Preprint*). In addition to predisposing the kinetochore to merotelic attachments through impaired bridging fibers, thinning of k-fibers might ultimately be responsible for the inability to resolve merotelic attachments, which would be necessary to ensure proper segregation of kinetochores during anaphase (Dudka et al., 2018). Altogether, our results reveal that augmin is the leading nucleator of bridging fibers and suggest a delicate interplay of bridging and k-fibers in the maintenance of spindle organization, kinetochore tension and mitotic fidelity.

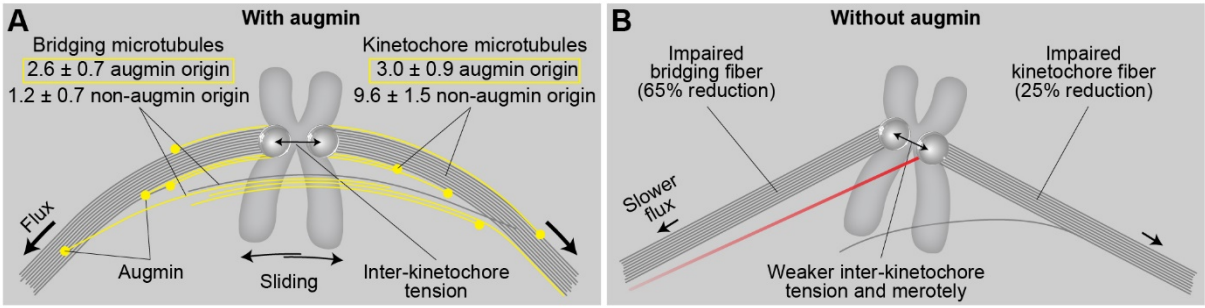


**Figure 6. A model of augmin-dependent nucleation of bridging microtubules with their contribution to forces acting on kinetochores and mitotic fidelity.** (A) Bridging microtubules are to a large extent formed by augmin-dependent nucleation. Within their overlaps microtubules slide apart, creating a pushing force onto the k-fibers, which produces tension between sister kinetochores and contributes to poleward flux of k-fibers. Augmin-nucleated microtubules (yellow) and microtubules nucleated through other pathways (gray) in bridging and k-fibers are shown together with the number of microtubules in each group, as estimated from HAUS6 depletion experiments (See Results). (B) Augmin depletion leads to a strong reduction of the microtubule number in bridging fibers and to a significant but smaller reduction in k-fibers, accompanied by slower poleward flux, weaker interkinetochore tension, and an increased tilt of kinetochore pairs. Impaired structure of bridging fibers and the increased tilt of kinetochores lead to a higher possibility of forming merotelic attachments.

## MATERIALS AND METHODS

**Cell lines.** Experiments were carried out using unlabeled human HeLa-TDS cells from the High-Throughput Technology Development Studio (MPI-CBG, Dresden); human HeLa-Kyoto BAC cells stably expressing PRC1-GFP, courtesy of Ina Poser and Tony Hyman (MPI-CBG, Dresden, Germany); human HeLa cells stably expressing CENP-A-GFP and Centrin1-GFP, which were a gift from Emanuele Roscioli and Andrew McAinsh (University of Warwick, Coventry, UK); human HeLa-TDS cells stably expressing GFP-α-tubulin as described in our previous work (Kajtez et al., 2016); human hTERT-RPE1 (hTERT immortalized retinal pigment epithelium) cells stably expressing CENP-A-GFP and human hTERT-RPE1 (hTERT immortalized retinal pigment epithelium) cells stably expressing both CENP-A-GFP and Centrin1-GFP, a courtesy of Alexey Khodjakov (Wadsworth Center, New York State Department of Health, Albany, NY, USA); human RPE1 CRISPR-Cas9 cells stably expressing PRC1-GFP, a gift from Thomas Surrey (Centre for Genomic Regulation, Barcelona, Spain); and human U2OS cells stably expressing CENP-A-GFP, mCherry-α-tubulin and PA-GFP-α-tubulin, a gift from Marin Barišić (Danish Cancer Society Research Center, Copenhagen, Denmark).

**Cell culture.** All cell lines were cultured in flasks in Dulbecco's Modified Eagle's Medium with 1 g/L D-glucose, pyruvate and L-glutamine (DMEM, Lonza, Basel, Switzerland), supplemented with 10% (vol/vol) heat-inactivated Fetal Bovine Serum (FBS, Sigma Aldrich, St. Louis, MO, USA) and penicillin (100 IU/mL)/streptomycin (100 mg/mL) solution (Lonza, Basel, Switzerland). For the selection of U2OS CENP-A-GFP mCherry-α-tubulin PA-GFP-α-tubulin, HeLa PRC1-GFP, HeLa CENP-A-GFP Centrin1-GFP and Hela GFP-α-tubulin cell lines, 50 µg/ml geneticin was added to the medium (Life Technologies, Waltham, MA, USA).

All cells were kept at 37°C and 5% $CO_2$ in a Galaxy 170 R humidified incubator (Eppendorf, Hamburg, Germany). They have also been regularly tested for mycoplasma contamination by examining the samples for extracellular DNA staining with SiR-DNA (100 nM, Spirochrome, Stein am Rhein, Switzerland) and Hoechst 33342 dye (1 drop/2 ml of NucBlue Live ReadyProbes Reagent, Thermo Fisher Scientific, Waltham, MA, USA) and have been confirmed to be mycoplasma free.

**Sample preparation and RNAi transfection**. At 80% confluence, DMEM medium was removed from the flask and cells were washed with 5 ml of PBS. Then, 1 ml 1% trypsin/EDTA (Biochrom AG, Berlin, Germany) was added to the flask and cells were incubated at 37°C and

5% $CO_2$ in a humidified incubator for 5 minutes. After the incubation, trypsin was blocked by adding 2 ml of DMEM medium. For RNAi experiments, the cells were seeded to reach 60% confluence the next day and cultured on 35 mm uncoated dishes with 0.16-0.19 mm (1.5 coverglass) glass thickness (MatTek Corporation, Ashland, MA, USA) in 2 mL DMEM medium with previously described supplements. After one day of growth, cells were transfected with either targeting or non-targeting siRNA constructs which were diluted in OPTI-MEM medium (Life Technologies, Waltham, MA, US) to a final concentration of 20 nM for HAUS6 and HAUS8 in medium with cells. HAUS6 and HAUS8 siRNA transfections were performed 48 hours prior to imaging and cotransfection with 100 nM Mad2 siRNA was additionally performed 24 hours prior to imaging using Lipofectamine RNAiMAX Reagent (Life Technologies, Waltham, MA, US) according to the instructions provided by the manufacturer. After four hours of treatment, the medium was changed to the previously described DMEM medium. The constructs used were human HAUS6 siRNA (L-018372-01-0005, Dharmacon, Lafayette, CO, USA), human HAUS8 siRNA (L-031247-01-0005, Dharmacon, Lafayette, CO, USA), human Mad2 siRNA (L-003271-00-0010, Dharmacon, Lafayette, CO, USA) and control siRNA (D-001810-10-05, Dharmacon, Lafayette, CO, USA). Mad2 was chosen instead of MPS1 inhibitors as it induces less segregation errors per cell in control cells, as well as to avoid a biased approach in which the inhibitor would likely be added at a different time point during an hours-long error correction process that occurs in augmin-depleted cells.

When microtubules were visualized during live cell-imaging in cell lines without stable expression of tubulin, staining was performed to a final concentration of 100 nM with a far-red silicon rhodamine (SiR)-tubulin-670 dye (Spirochrome, Stein am Rhein, Switzerland), 45 minutes to 2 hours prior to imaging. As for DNA, either SiR-DNA or SPY-555-DNA (Spirochrome, Stein am Rhein, Switzerland) were used to a final concentration of 100 nM, 20 minutes to 2 hours prior to imaging. In order to avoid dye efflux, a broad-spectrum efflux pump inhibitor verapamil (Spirochrome, Stein am Rhein, Switzerland) was added at a final concentration of 0.5 μM to RPE1 cells along with tubulin and/or DNA dyes. As an additional control for metaphase cells, MG-132 (Sigma Aldrich, M7449-1ML, MO, USA) was added to the cells used for the measurement of spindle size for 30 minutes prior to imaging at a final concentration of 20 μM.

**Immunofluorescence.** For confocal imaging, HeLa cells stably expressing PRC1-GFP were grown on glass-bottom dishes (14 mm, No. 1.5, MatTek Corporation) and fixed by 2 ml of ice-cold methanol for 1 min at -20°C. Following fixation, cells were washed 3 times for 5 minutes

with 1 ml of PBS and permeabilized with 0.5% Triton-X-100 in water for 15 minutes at a room temperature. This step was repeated twice when tubulin staining was performed. To block unspecific binding, cells were incubated in 1 ml of blocking buffer (1% normal goat serum (NGS)) for 1 hour at 4°C. Cells were then washed 3 times for 5 minutes with 1 ml of PBS and incubated with 250 µl of primary antibody solution overnight at 4˚C. The primary antibodies used were as follows: rabbit polyclonal PRC1 (diluted 1:100, sc-8356, Santa Cruz Biotechnology), rabbit polyclonal HAUS6 (diluted 1:250, ab-150806, Abcam), rabbit polyclonal HAUS8 (diluted 1:100, PA5-21331, Invitrogen) and rat monoclonal tubulin (diluted 1:100, MA1-80017, Invitrogen). After the incubation with a primary antibody, cells were washed 3 times for 5 minutes with 1 ml of PBS and then incubated with 250 µl of secondary antibody for 45 minutes at a room temperature. Alexa Fluor 488 and 594 (Abcam) were used as secondary antibodies at a 1:1000 dilution for PRC1 staining, 1:500 dilution for HAUS6 and 1:250 for HAUS8 and tubulin staining. DAPI (1 µg/mL) was used for chromosome visualization.

For STED imaging, RPE1 cells stably expressing CENP-A-GFP were grown on glass-bottom dishes (14 mm, No. 1.5, MatTek Corporation), cell medium was removed, and cytoskeleton extraction buffer was added for 20 seconds to remove the components of the cytoplasm. Following extraction, cells were fixed in 3% paraformaldehyde and 0.1% glutaraldehyde solution for 10 minutes. To reduce the background fluorescence, quenching (100 mM glycine in PBS) and reduction (0.1% sodium borohydride in PBS) solution were added for 7 and 10 minutes, respectively. To prevent non-specific binding, cells were incubated in blocking/permeabilization buffer (2% normal goat serum and 0.5% Triton-X-100 in PBS) for 2 hours at 4°C. Microtubules were then stained using a rat anti-tubulin primary antibody solution (diluted 1:500 in blocking/permeabilization buffer, MA1-80017, Invitrogen) with a 4°C overnight incubation. The next day, cells were washed with PBS three times for 5 minutes. After washing, a secondary antibody Alexa Fluor 594 (dilution 1:1000, Abcam) was added and incubated for 1 hour at room temperature. Additionally, DAPI (1 µg/mL) was added and incubated for 15 minutes at room temperature to visualize chromosomes. Cells exposed to cold treatment were incubated with cold media on ice for 13 min prior to extraction of cytoplasmic components.

**Immunoblotting.** RPE1 cells stably expressing CENP-A-GFP and Centrin1-GFP and HeLa cells stably expressing PRC1-GFP were grown on six-well plates (Greiner Bio-one) and subjected to HAUS6 or HAUS8 siRNA treatment as indicated before. Following transfection,

cells were lysed in RIPA buffer (R0287, Sigma) containing 1x protease inhibitor (5892970001, Roche), 1x phosphatase inhibitor (4906837001, Roche) and 1mM PMSF by two cycles of freezing and thawing in liquid nitrogen. Protein extracts were mixed with 2x Laemlli sample buffer (S3401, Sigma) and heated at 95˚C for 10 minutes prior to SDS-PAGE. After protein transfer onto the nitrocellulose membrane (IB23002, Invitrogen) and blocking with blocking solution (5% bovine serum albumin and 0,1% Tween 20 in PBS) for 1 hour, membranes were incubated overnight at 4˚C with primary antibodies diluted in blocking solution. The primary antibodies used were as follows: rabbit polyclonal HAUS6 (diluted 1:1000, ab-150806, Abcam), rabbit polyclonal GAPDH (diluted 1:1000, ab9485, Abcam). Rabbit polyclonal HAUS8 antibody (diluted 1:1000, PA5-21331, Invitrogen and NBP2-42849, Novus Biologicals) resulted in no detectable bands under these conditions. Membranes were washed with 0.1% Tween 20 in PBS, incubated for 1 hour with anti-rabbit HRP-conjugated secondary antibodies (dilution 1:10000, ab6721) and visualized on the C-DiGit blot scanner (LI-COR, Bad Homburg, Germany) with WesternSure PREMIUM Chemiluminescent Substrate (926-95000, LI-COR).

**Microscopy.** STED microscopy of fixed cells and live-cell imaging of anaphase were performed using an Expert Line easy3D STED microscope system (Abberior Instruments, Göttingen, Germany) with the 100x/1.4NA UPLSAPO100x oil objective (Olympus, Tokio, Japan) and an avalanche photodiode (APD) detector. The 488 nm line was used for excitation in both cases, with the addition of the 561 nm line for excitation and the 775 nm laser line for depletion during STED superresolution imaging. Images were acquired using the Imspector software. The xy pixel size for fixed cells was 20 nm and 6 focal planes were acquired with 300 nm distance between planes were acquired. For confocal live-cell imaging of anaphase, the xy pixel size was 80 nm and 16 focal were acquired, with 1 µm distance between the planes and 30 s time intervals between different frames.

Other confocal images and videos were acquired using a previously described microscope setup (Buđa et al., 2017), consisting of a Bruker Opterra Multipoint Scanning Confocal Microscope (Bruker Nano Surfaces, Middleton, WI, USA), mounted on a Nikon Ti-E inverted microscope with a Nikon CFI Plan Apo VC 100x/1.4 numerical aperture oil objective (Nikon, Tokyo, Japan). During live-cell imaging, cells were kept at 37°C and 5% $CO_2$ in Okolab Cage Incubator (Okolab, Pozzuoli, NA, Italy). To excite Hoechst, GFP, mCherry or SiR fluorescence, a 405 nm, 488 nm, 561 nm or 647 nm laser lines were used, respectively. Opterra Dichroic and Barrier Filter Set 405/488/561/640 enabled the separation of excitation light from the emitted

fluorescence. Images were acquired using Evolve 512 Delta Electron Multiplying Charge Coupled Device (EMCCD) Camera (Photometrics, Tuscon, AZ, USA), with camera readout mode of 20 MHz. The xy pixel size was 83 nm. In all experiments where the whole spindle stack was imaged, z-stacks were acquired with unidirectional xyz scan mode at 37 focal planes and 0.5 µm distance between the planes. Photoactivation was performed perpendicular to pole-to-pole axis of metaphase spindles using a 405-nm laser diode (Coherent, Santa Clara, CA, USA) and a line pattern of 12 equally distributed points, with each point representing one laser hit. The interval between the points was 0.05 ms and photoactivation area was set to 0.5 µm for each point. The interval between successive frames was set to 10 s and one central z-plane was imaged.

**Image processing and data analysis.** In cells where HAUS6 or HAUS8 were silenced only bipolar metaphase spindles were imaged and analyzed, even though multipolar spindles were observed as reported previously (Lawo et al., 2009). All images were analyzed in Fiji/ImageJ (National Institutes of Health, Bethesda, MD, USA). Raw images were used for quantification and contrast was adjusted for clarity for representation on figures. MatLab (MathWorks, Natick, MA, USA) was used for calculations and plotting and Rstudio (R Foundation for Statistical Computing, Vienna, Austria) to transform the cells into an end-on view. Figures were assembled in Adobe Illustrator CS5 (Adobe Systems, Mountain View, CA, USA).

**Measuring the bridging fiber intensity.** For the analysis based on small square regions which was performed on both STED and confocal images, tubulin intensity in bridging and k-fibers was measured using either a 25x25 or 5x5 pixel Square tool (ImageJ) on STED and confocal images, respectively. To measure bridging fibers, the square was positioned on the fiber spanning the area between two kinetochores. K-fibers were measured right next to the kinetochores. The average intensity of the two sister k-fibers was used for further analyses. The background was measured using the same tool at several empty areas within the spindle and its average was subtracted from bridging ($I_b = I_{b+bcg} - I_{bcg}$) and k-fiber intensities ($I_k = I_{k+bcg} - I_{bcg}$). 10 randomly positioned empty areas were taken into account while calculating background for STED imaging, whereas 2 empty areas just above and below bridging fiber were taken into account while calculating background for confocal imaging due to different nature of the acquired images. All measurements were performed on randomly selected bundles in single z-planes, after determining that no other microtubules were crossing the area of measurement. In STED images, the intensity of astral microtubules was additionally measured using the 25x25 pixel Square tool (ImageJ). Their background was measured using the same tool in the empty

area between the two astral microtubules and it was subtracted from astral microtubule intensity ($I_a$=$I_{a+bcg}$-$I_{bcg}$).

On top of that, tubulin intensities of the bridging fiber and k-fiber region in confocal images were measured in a single z plane using the Segmented Line tool by drawing a 5 pixel line (ImageJ) along the contour of k-fibers and the corresponding bridging fiber. Background was measured in the same z plane by drawing the 5 pixel thick line along the length of the metaphase midzone, as this represents the background signal caused by the presence of neighboring microtubules. The minimum value of the midzone intensity profile was subtracted from the intensity profiles of bundle contours. The minimum value of the mean tubulin intensity profile was set as a distance of zero µm and was selected as the center of the bridging fiber. The final intensity of a bridging fiber ($I_b$) was calculated as the mean value of intensities in the area 500 nm around the center of the bridging fiber. The final intensity of a k-fiber region ($I_{bk}$), which also includes the bridging fiber, was calculated as an average of two mean values of intensities in the area 500 nm around the distance of 1.5 µm away from the center of the bridging fiber. The intensity value of k-fibers alone ($I_k$) was then calculated as $I_k = I_{bk} - I_b$.

**Comparison of SiR- and GFP-tubulin signal.** For the comparison of SiR and GFP-tubulin signal in HeLa cells stably expressing GFP-α-tubulin, the previously described analysis was used. Tubulin intensity of the bridging fiber and k-fiber region was measured in a single z plane using the Segmented Line tool in ImageJ by drawing the 5 pixel line along the contour of k-fibers and the corresponding bridging fiber. Due to high noise, only outermost bundles were taken into analysis and the reduction was not calculated. The background was measured in the same z plane by drawing the 5x5 pixel square in the cytoplasm and was subtracted from the bundle intensity profiles. The minimum value of the intensity profile was set as a distance of zero µm and was selected as the center of the bridging fiber.

**The interkinetochore distance.** To calculate the interkinetochore distance, two points were put on the centers of signal in each kinetochore pair using a Point tool in ImageJ. Additionally, two points were put on spindle poles and two points on the upper and lower edge of the metaphase plate. Interkinetochore distance and distance from spindle axes were calculated using a home-written MatLab script. Two-dimensional analysis was applied when all tracked kinetochore pairs resided within 2 µm around the central z-plane. Three-dimensional analysis was used when all kinetochore pairs in the spindle were taken into account, regardless of their position. In 3D analysis, the exact distance from the long spindle axis (c) was calculated using the Pythagorean theorem, where a = projected distance of a middle point between two sister

kinetochores in a particular z-plane from the long spindle axis, b = distance between the central z-plane and the z-plane of the kinetochore pair x 0.81 (correction factor for the oil objective only, see Transformation of spindles into an end-on view). Kinetochore pairs were defined as those in the inner or the outer part of the spindle if their distance to the pole-to-pole axis was smaller or larger than the average distance of all tracked kinetochore pairs to the pole-to-pole axis, respectively. Additionally, kinetochores with visible bridging fibers and kinetochores with no visible bridging fibers were separately tracked and analyzed in confocal images of RPE1 cells stably expressing CENP-A-GFP and Centrin1-GFP, where the presence of bridging fibers was determined by measuring intensity profiles of the tubulin signal between two kinetochores.

**Transformation of spindles into an end-on view.** Z-stacks of the mitotic spindles that were positioned horizontally were transformed into the end-on view using a home-written R script previously described in our work (Novak et al., 2018). Prior to transformation, a single-channel grayscale z-stack was rotated using ImageJ to make the long axis of the spindle parallel to the x-axis. Signal intensity at each pixel was used to obtain an end-on view of the spindles by applying the following transformation: I' (i · pixel size, j · pixel size, k · z-distance) = I (k · z-distance, i · pixel size, j · pixel size). A correction factor of 0.81 was used for the z-distance to correct for aberrations caused by the different refractive index mismatch of aqueous samples and immersion oil (Novak et al., 2018).

**Number of bundles.** The number of bundles in HeLa and RPE1 PRC1-GFP cells was determined in an end-on view of the spindle by using sum intensity projections of 10 central z-planes covering 0.83 µm along the long spindle axis.

**Spindle length, width and metaphase plate diameter**. Spindle length, width and metaphase plate diameter were measured on maximum intensity projections of the side view z-stack of spindles. Spindle length was determined as a distance between the two poles. The position of the poles was determined as either the center of Centrin1 signal or the outermost points of the tubulin or PRC1 signal at the spindle pole. Spindle width was measured as the distance between two lines parallel to the long axis of the spindle and encompassing the outermost PRC1- or tubulin-labeled bundles. Additionally, in RPE1 cells stably expressing CENP-A-GFP and Centrin1-GFP the metaphase plate diameter was measured as the distance between the outermost kinetochore pairs, whereas in HeLa PRC1-GFP it was measured as the distance between the outermost chromosome ends.

**Overlap length.** Overlap length was measured on sum intensity projections of 2 to 4 z-planes covering the entire bundle of interest, using ImageJ Segmented line tool by drawing a pole to pole line along the contour of PRC1-GFP and acquiring an intensity profile. The overlap length was defined as the length of the base of the PRC1-GFP intensity peak (Polak et al., 2017).

**PRC1 intensity.** PRC1 intensity was measured in sum intensity projections of 10 central z-planes of the spindle. Total PRC1 signal in the cell was marked by using Polygon selection tool (ImageJ) and 5x5 Square tool was used to determine the background in the cytoplasm. The final intensity values were obtained using the following formula: PRC1 intensity = Integrated Density of the spindle – (Area of selected cell x mean fluorescence of background). Intensity profiles of PRC1-GFP were measured on the sum intensity projections of 10 central z-planes in an end-on view of the spindle by drawing a 50 pixel wide Straight line tool across the diameter of the spindle.

**Spindle shape.** The shape of spindles was determined in ImageJ using a Point tool. Ten points were distributed throughout the bundle, with the first and last point positioned at the spindle poles. The images were rotated to make the long spindle axis parallel to the x axis. In control cells, only the outermost bundle was tracked. In HAUS6 siRNA treated cells, three different groups of outermost bundles were tracked: bundles with visible bridging fibers, bundles with no visible bridging fibers and curved bundles extending far from the metaphase plate. Shape and curvature were calculated using a home-written MatLab script by fitting a circle to the tracked points along the bundle. Contour lengths of the bundles were measured by calculating the cumulative distance between the first and the last point of the tracked bundle.

**Poleward flux rate.** For measuring the poleward flux rate, 10-pixel wide line was drawn from pole to pole along the bundle with photoactivation signal that lasted at least 5 time frames (40 s), using the Segmented Line tool in ImageJ. The position of photoactivated mark in each time frame was determined as the distance between the peaks of intensity profiles in photoactivation and SiR-tubulin channels for photoactivation mark and closer spindle pole, respectively. The analysis was performed on images processed with Gaussian Blur filter with Sigma set to 2 to improve the definition of the intensity profile peaks.

**Tracking and classification of segregation errors**. Three types of segregation errors were analyzed in Mad2-depleted and Mad2/HAUS6-codepleted anaphase spindles: misaligned kinetochores, lagging kinetochores and other errors. Misaligned kinetochores were defined as those in which both kinetochores of the pair were situated outside the metaphase plate 30 s

before anaphase onset. Lagging kinetochores were defined as those in which the CENP-A signal was visibly stretched and the kinetochore was situated in the central part of the spindle, outside the kinetochore mass that was moving towards the pole during anaphase. Finally, segregation errors classified as others included various kinetochores, precise classification of which was impossible using only CENP-A signal. These included kinetochores situated outside the moving kinetochore mass without stretched CENP-A signal, kinetochore pairs that remained completely unseparated for the whole duration of anaphase, as well as kinetochore pairs in which both kinetochores remained non-stretched and in the central part of the spindle despite the initial separation. Segregation errors were further divided based on their distance to the pole-to-pole axis into those in the inner and the outer part of the spindle. The distance of the kinetochore pair from the pole-to-pole axis was determined in 3D using a home written Matlab script, and the obtained value was then normalized to spindle half-width determined using maximum intensity projections in ImageJ. All kinetochores situated in the area less than 0.5 from the spindle axis 30 s before anaphase onset were defined as those in the inner part of the spindle and all kinetochore pairs in the area equal to or above the value of 0.5 were defined as kinetochores in the outer part of the spindle. All kinetochore pairs were manually tracked in time from just before anaphase onset until entering the daugther cell by using the Point tool in ImageJ. In images acquired using STED microscopy, merotelic attachments were defined as those in which one kinetochore forms attachments with microtubules from the opposite side of the spindle, with no visible microtubule signal just below or above the kinetochore.

**Anaphase A and B speed**. To measure anaphase A speed, the coordinates of kinetochores and poles were tracked in time using the Point tool in ImageJ. The speed was calculated from the time point when the distance between the kinetochore and its closer pole started gradually decreasing. The slope of a line equation obtained from the linear fitting of distances over time was determined for every kinetochore as the anaphase A speed. Anaphase B speed was calculated in a manner similar to anaphase A, but instead of kinetochores, the positions of poles were tracked in time with the first time frame determined as the frame when the distance between two poles started gradually increasing.

**Measuring the tilt of kinetochores at anaphase onset**. Anaphase onset was determined in a frame just before the interkinetochore distance of the tracked kinetochore pair started gradually increasing. The coordinates of kinetochore pairs that ended up as errors and of error-free kinetochore pairs were tracked along with the coordinates of spindle poles. The angle that the kinetochores form with the long spindle axis was calculated using a home written Matlab script.

**Acknowledgements**

We thank Alexey Khodjakov for the hTERT-RPE1 CENP-A-GFP and the hTERT-RPE1 CENP-A-GFP Centrin1-GFP cell line, Ina Poser and Tony Hyman for the HeLa PRC1-GFP cell line, Thomas Surrey for the RPE1 PRC1-GFP cell line, Emanuele Roscioli and Andrew McAinsh for the HeLa CENP-A-GFP Centrin1-GFP cell line, Mariola Chacon for the HeLa-TDS cell line and Marin Barišić for the U2OS CENP-A-GFP mCherry-α-tubulin PA-GFP-α-tubulin cell line. We also thank Marko Šprem and Abberior team for help with developing microscopy protocols, Ivana Štimac for help with creating the MatLab scripts, Josip Čačković and Arian Ivec for technical assistance with the initial experiments and calculations, all members of Tolić and Pavin groups for discussions and advice, Ivana Šarić for the drawings, and the reviewers for constructive feedback. This work was funded by the European Research Council (ERC Consolidator Grant, GA number 647077 and ERC Synergy Grant, GA number 855158), Croatian Science Foundation (Project IP-2014-09-4753), Croatian Science Foundation Cooperation Programme with Croatian Scientists in Diaspora "Research Cooperability" (Project PZS-2019-02-7653), and QuantiXLie Centre of Excellence, a project cofinanced by the Croatian Government and European Union through the European Regional Development Fund - the Competitiveness and Cohesion Operational Programme (Grant KK.01.1.1.01.0004).

**Author Contribution**

V.Š. and I.K. performed all experiments, except pilot experiments and those on PRC1 distribution in HeLa cells, which were performed by M.M. in the initial phase of the project. I.K. and V.Š. analyzed the data, assembled the figures, and wrote the manuscript with input from I.M.T., who supervised the project with J.S. co-supervising the initial phase.

**Competing Interests**

The authors declare no competing interest.

**Data Availability**

All data are available from the corresponding author upon request.

**Code Availability**

All scripts used in this study are available upon request.

## Supplementary Figures

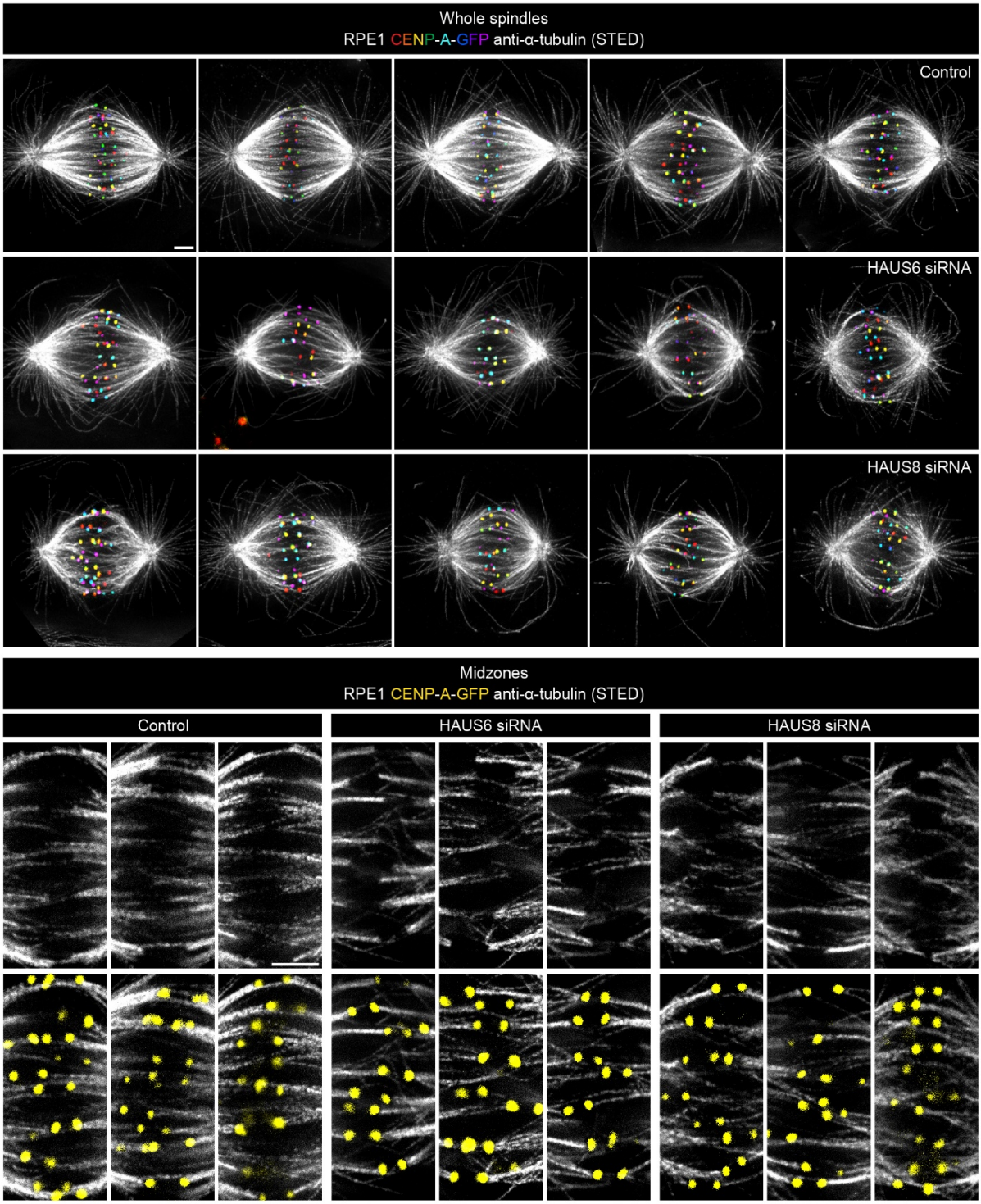


**Supplementary Figure 1 (S1).** Panels with whole spindles: STED superresolution images of microtubules immunostained for α-tubulin (gray) in control (top), HAUS6- (middle) and HAUS8-depleted (bottom) RPE1 cells stably expressing CENP-A-GFP (rainbow, confocal). Images show maximum intensity projections of 6 central z-planes of metaphase spindles. The kinetochores are color-coded for depth from blue to red with the Spectrum LUT in ImageJ. Panels with midzones: insets of STED superresolution images of microtubules (gray) from spindle midzones in control (left), HAUS6- (middle) and HAUS8-depleted (right) RPE1 cells stably expressing CENP-A-GFP (yellow). Top row shows only microtubules present in the

midzone area and bottom row shows the same midzones with the kinetochores. Images show single z-plane and do not correspond to midzones of spindles in the panel with whole spindles. All images are adjusted for clarity based on the intensity of astral microtubules in each image. Scale bars, 2 µm.

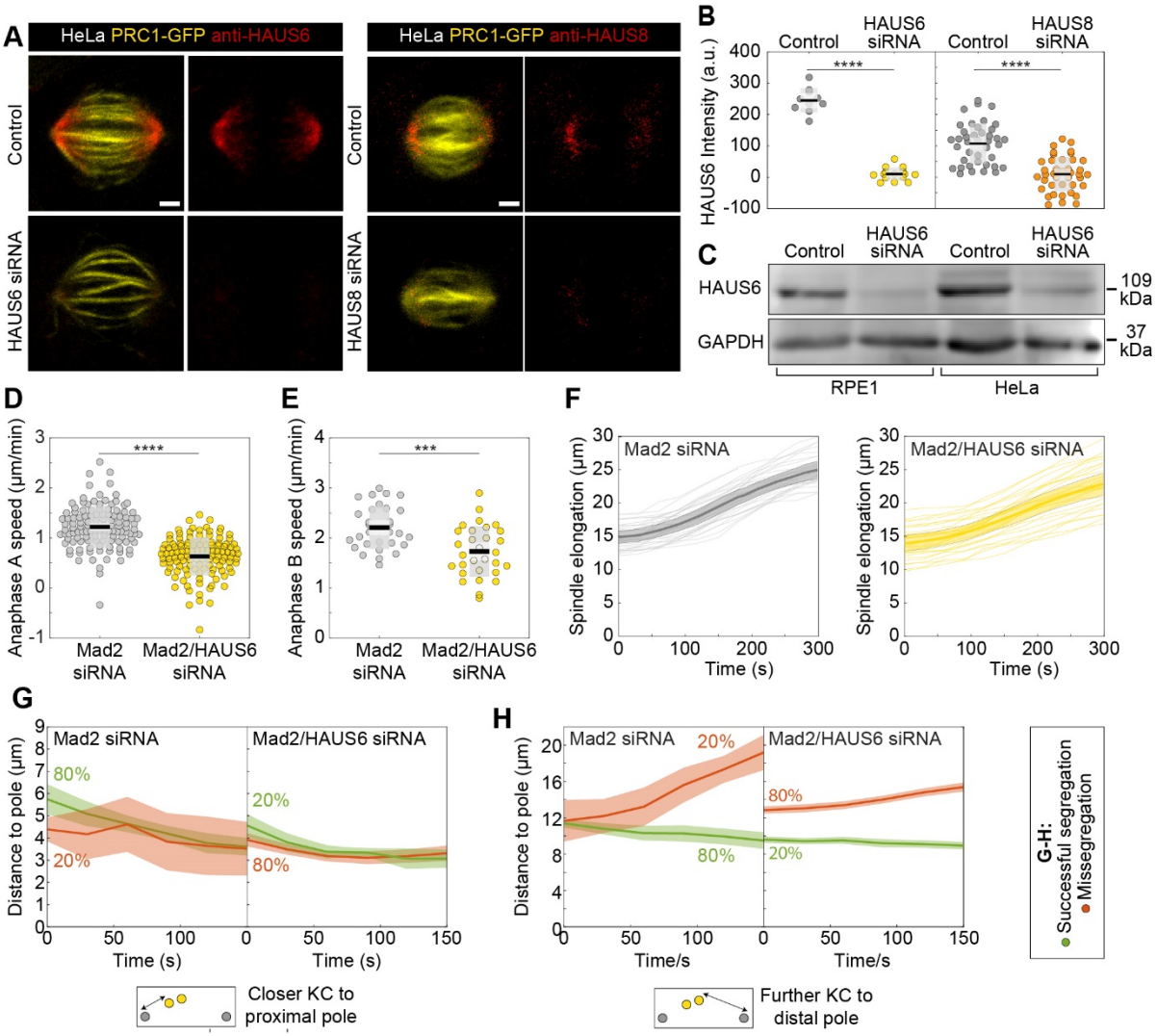


**Supplementary Figure 2 (S2).** (A) Fixed control, HAUS6 and HAUS8 siRNA-treated HeLa cells stably expressing PRC1-GFP (yellow) and immunostained for HAUS6 (red, left panels) or HAUS8 (red, right panels). Chromosomes were stained with DAPI (not shown) to identify cells in metaphase. Images are sum intensity projections of nine central z-planes. (B) Univariate scatter plot of HAUS6 and HAUS8 intensities in control cells (gray) and cells depleted of HAUS6 (yellow) or HAUS8 (orange). The intensity of HAUS6 and HAUS8 in siRNA-treated cells is reduced by 96 ± 2% and 82 ± 16% compared to control cells, respectively. (C) Immunoblot analysis of HAUS6 siRNA treatment efficiency in RPE1 cells stably expressing CENP-A-GFP and Centrin1-GFP and HeLa cells stably expressing PRC1-GFP. HAUS6 antibody was used to validate the efficiency of knockdown, with GAPDH as the loading control. The representative image of three independent experiments is shown. (D) Univariate scatter plot of anaphase A speed, defined as the distance of kinetochore and the closer pole in time, for Mad2-depleted (gray) and Mad2/HAUS6-codepleted cells (yellow). The anaphase A speed in Mad2-depleted cells is 1.2 ± 0.04 µm/min, and in Mad2/HAUS6 codepleted cells 0.6 ± 0.03

µm/min. N = 120 kinetochores from 30 cells in both treatments. (E) Univariate scatter plot of anaphase B speed, defined as the distance between two poles in time, for Mad2-depleted (gray) and Mad2/HAUS6-codepleted cells (yellow). The anaphase B speed in Mad2-depleted cells is 2.2 ± 0.08 µm/min, and in Mad2/HAUS6-codepleted cells 1.7 ± 0.09 µm/min. N = 31 Mad2-depleted cells and N = 30 Mad2/HAUS6-codepleted cells. (F) A plot of spindle elongation in time following Mad2 depletion (gray) and Mad2/HAUS6 (yellow) codepletion. (G) A plot of distance of the misaligned kinetochore that is closer to the proximal pole in time following Mad2 depletion (left) and Mad2/HAUS6 (right) codepletion. (H) A plot of distance of the misaligned kinetochore that is further away from the proximal pole in time following Mad2 depletion (left) and Mad2/HAUS6 (right) codepletion. Kinetochore pairs in (G) and (H) are divided based on their outcome in anaphase into those that successfully segregated (green) and those that missegregated (red). Insets show schematic representations of the distance of closer and further kinetochore (yellow) to their corresponding spindle pole (gray). (B, D and E) Boxes represent standard deviation (dark gray), 95% confidence interval of the mean (light gray) and mean value (black). (F-H) Values are shown as mean (thick line) and SEM (shaded area). All results were obtained from three independent experiments. Statistical analysis (B and E) t-test; (D) Mann-Whitney U test; p-value legend: < 0.0001 (****), 0.0001 to 0.001 (***), 0.001 to 0.01 (**), 0.01 to 0.05 (*), ≥ 0.05 (ns). Scale bars, 2 µm.

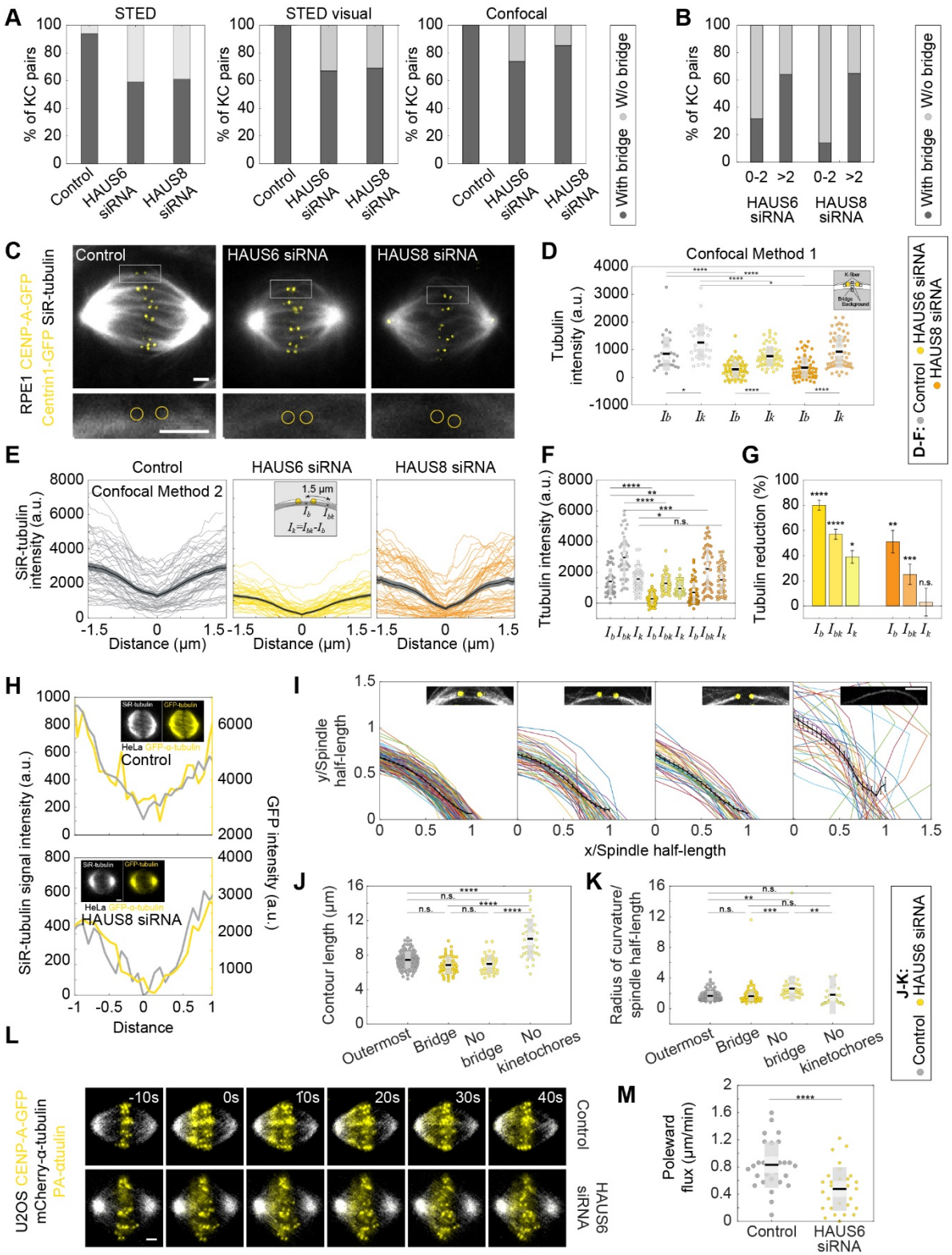


**Supplementary Figure 3 (S3).** (A) The fractions of kinetochore pairs with bridging fibers (dark gray) and with undetectable bridging fibers (light gray). The fractions are obtained from the tubulin intensity measured in STED images (left), by visual inspection of STED images (middle) and from SiR-tubulin intensity measured in confocal images (right) of control, HAUS6- and HAUS8-depleted cells. (B) The fractions of kinetochore pairs with bridging fibers (dark gray) and without bridging fibers (light gray) depending on the projected distance from the long (pole-to-pole) spindle axis in confocally imaged HAUS6- (left) and HAUS8- (right)

depleted cells. (C) Live images (single z-plane) of SiR-tubulin (gray) stained metaphase spindles in control (left), HAUS6- (middle) and HAUS8-depleted (right) RPE1 cells stably expressing CENP-A-GFP and Centrin1-GFP (both in yellow). The enlarged boxes show bridging fibers affected by HAUS6 or HAUS8 depletion compared to the bridging fiber in control cell. The positions of kinetochores are marked with yellow circles. (D) Univariate scatter plot of the tubulin signal intensities of bridging and k-fibers in control (gray), HAUS6- (yellow) and HAUS8-depleted (orange) RPE1 cells stably expressing CENP-A-GFP and Centrin1-GFP. Schematic representation of the method for measuring tubulin intensity of a bridging fiber and corresponding k-fibers (kinetochores are shown in yellow and tubulin signal in white). For the analysis, the average of two k-fibers is calculated and the average of background is subtracted from the tubulin intensity values of the bridging and k-fiber. N = 30 bridging and sister k-fibers in 10 control cells and N= 60 bridging and sister k-fibers in both HAUS6- and HAUS8-depleted cells. (E) Intensity profiles of SiR-tubulin signal along the bundles in control cells (gray) and after HAUS6 (yellow) or HAUS8 (orange) depletion. The center of the bridging fiber is set at a distance zero and the minimum intensity of the central part of the spindle was subtracted from the values of intensity profiles. N = 10 cells and 50 bundles for control and HAUS6 siRNA-treated cells, N = 10 cells and 48 bundles for HAUS8 siRNA-treated cells. Mean ± SEM (thick black line and shaded area, respectively). The method for measuring the tubulin intensity of the bridging fiber and the corresponding k-fibers is depicted in the inset; the average of two k-fibers was calculated whenever both k-fibers resided in the same-z plane. (F) Univariate scatter plot of the tubulin signal intensities of the bridging fiber (Ib), the bundle consisting of the k-fiber and bridging fiber (Ibk), and k-fiber (Ik) in control (gray), HAUS6- (yellow) and HAUS8-depleted (orange) cells. (G) Reduction of the tubulin signal in the bridging fiber (Ib), the bundle consisting of the k-fiber and bridging fiber (Ibk), and the k-fiber (Ik) following HAUS6 (yellow) or HAUS8 (orange) depletion. Values are shown as mean ± SEM. P-values were calculated using the absolute values of tubulin signal intensity of bridging or k-fibers following HAUS6 or HAUS8 depletion, compared to the absolute values of tubulin signal intensity of corresponding fibers in control cells. (H) Intensity profiles of SiR-tubulin (gray) and GFP-tubulin (yellow) signal in HeLa cells stably expressing GFP-α-tubulin (yellow) and stained with SiR-tubulin (gray). The values of two intensity profiles are adjusted to observe the level of overlapping between them and the minimum of the SiR-tubulin signal is set as a distance zero. This method was used as a control to validate SiR-tubulin labeling. (I) Bundle contours from RPE1 cells stably expressing CENP-A-GFP (yellow). Examples of each bundle type are shown in insets. From left to right: the outermost bundle in control cells, the outermost bundle with a bridging fiber, the outermost bundle without a bridging fiber and the outermost bundle without kinetochores in HAUS6-depleted cells; mean ± SEM is shown in black. (J) Univariate scatter plot of contour lengths and (K) radii of curvature in control (gray), HAUS6- (yellow) and HAUS8-depleted (orange) cells. N = 120 outermost bundles from 30 control cells, 54 bundles with a bridging fiber, 40 bundles without a bridging fiber, and 36 bundles without kinetochores from 30 HAUS6-depleted cells. (L) Time-lapse images of control (top) and HAUS6-depleted (bottom) U2OS cells stably expressing CENP-A-GFP (yellow), mCherry-α-tubulin (gray) and PA-GFP-α-tubulin, before (-10 s), at the time when photoactivation (yellow) was performed (0 s), and after photoactivation. (M) Univariate scatter plot of the poleward flux speed in control cells (gray) and after HAUS6 depletion (yellow). N = 30 measured photoactivation spots in 30 cells for both conditions. (D, F, J, K and M) Boxes represent standard deviation (dark gray), 95% confidence interval of the mean (light gray) and mean value (black). All results were obtained from three independent experiments. Statistical analysis; (D, F, G, J and K) ANOVA with post-hoc Tukey test; (M) t-test, p-value legend: < 0.0001 (****), 0.0001 to 0.001 (***), 0.001 to 0.01 (**), 0.01 to 0.05 (*), ≥ 0.05 (ns). Scale bars, 2 µm.

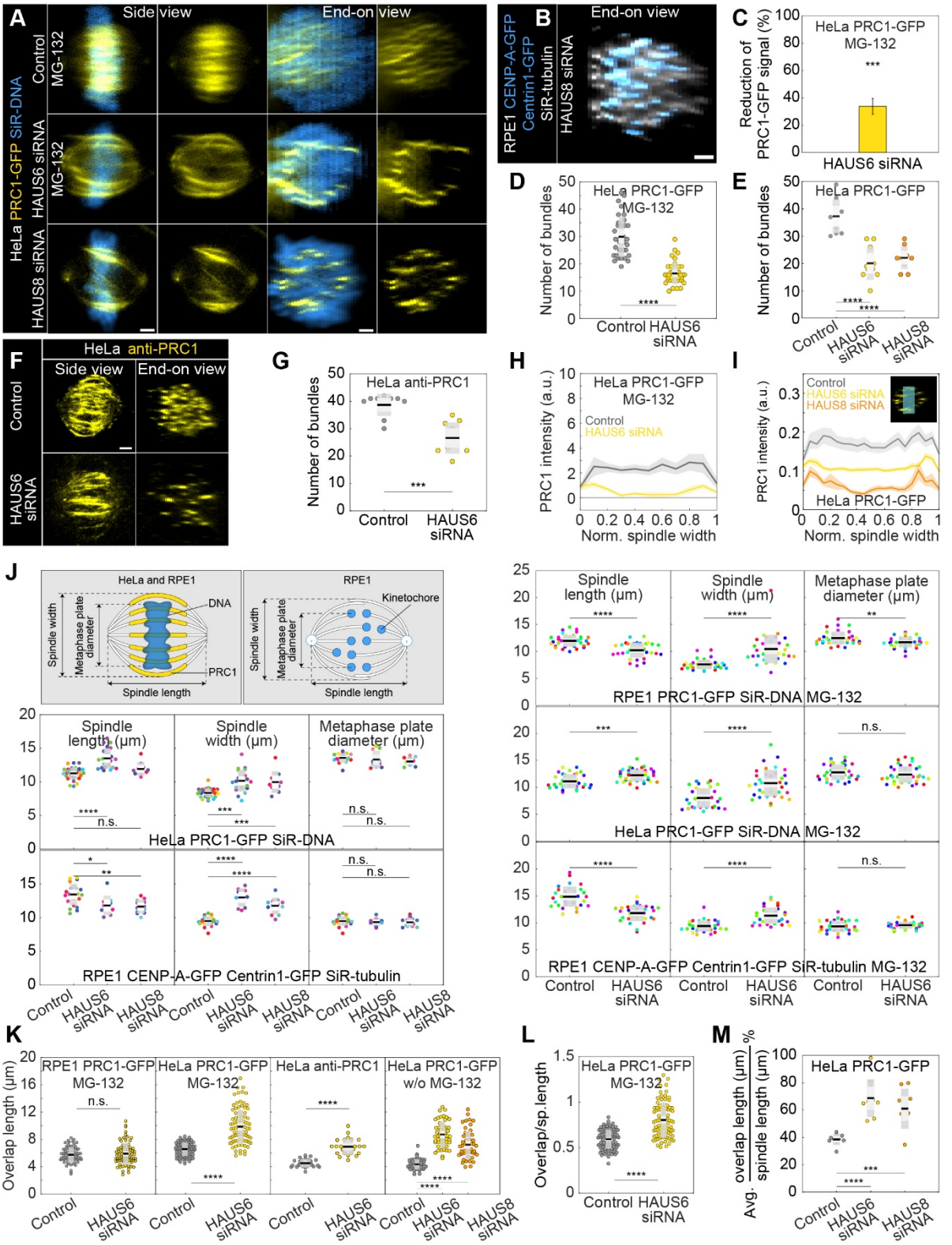


**Supplementary Figure 4 (S4).** (A) Four columns represent live images of metaphase spindles in HeLa cells stably expressing PRC1-GFP (yellow) and stained with SiR-DNA (blue) in control (top) and after HAUS6 (middle) or HAUS8 (bottom) depletion. Control and HAUS6-depleted cells are treated with MG-132. 1st and 2nd column: side view of the spindle; 3rd and 4th column: end-on view of the same spindle, showing a barrel-like arrangement of PRC1-labeled bundles after augmin depletion. Side views are sum projections of 5 central z-slices

(Δz=0.5 μm) and end-on views are sum projections of 10 central z-slices (Δz=0.083 μm). (B) End on view of RPE1 cell stably expressing CENP-A-GFP and Centrin1-GFP (both in blue) and stained with SiR-tubulin (gray) after HAUS8 depletion. End-on view is a sum projection of 10 central z-slices (Δz=0.083 μm). (C) Reduction of the PRC1 signal in HeLa cells stably expressing PRC1-GFP and treated with MG-132, measured in sum intensity projection of 10 central z-slices following HAUS6 depletion. Values are shown as mean ± SEM. P-values were calculated using the absolute values of the PRC1 signal intensity following HAUS6 depletion (N = 39 cells), compared to the absolute values of the PRC1 signal intensity in control cells (N = 33 cells). (D) Univariate scatter plot of the number of PRC1-labeled bundles in HeLa cells stably expressing PRC1-GFP treated with MG-132, counted in the end-on view of the spindle in control (gray) and HAUS6-depleted cells (yellow). N = 32 control and 39 HAUS6-depleted cells. (E) Univariate scatter plot of the number of PRC1-labeled bundles in HeLa cells stably expressing PRC1-GFP, counted in the end-on view of the spindle in control (gray), HAUS6- (yellow) and HAUS8-depleted (orange) cells without MG-132 treatment. N = 10 cells for all conditions. (F) Fixed control and HAUS6 siRNA-treated HeLa cells immunostained for PRC1 (yellow). Images are sum intensity projections of 5 central z-planes in a side view and sum projection of 10 central z-planes in an end-on view. The corresponding number of PRC1-labeled bundles (G) is shown in an univariate scatter plot. N = 10 control and 10 HAUS6-depleted cells. (H) The PRC1-GFP intensity profile in HeLa cells stably expressing PRC1-GFP and treated with MG-132, measured in the end-on view of the spindle in control cells (gray) and after HAUS6 (yellow) depletion. The blue line in the inset marks the measured region (width: 2.5 μm). Mean (thick lines) and SEM (shaded areas). (I) Same as (H) but cells are not treated with MG-132 and HAUS8 depletion (orange) is included in the plot. (J) Schematic representations of spindle geometry measurements in RPE1 and HeLa cells stably expressing PRC1-GFP (yellow) and stained with SiR-DNA (blue) and RPE1 cells stably expressing CENP-A-GFP and Centrin1-GFP (both in yellow) and stained with SiR-tubulin (white). Univariate scatter plots of the spindle length (left), width (middle) and diameter of the metaphase plate (right) are shown in this order on both left and right panels. The cell type from which the measurement was obtained is indicated in each panel. The measurements were taken in control, HAUS6- or HAUS8-depleted cells. Left panels show cells treated with MG-132 and right panels represent untreated cells. Each color in the plot corresponds to data obtained in one cell. N = 36 control cells and 33 HAUS6-depleted cells following MG-132 treatment of the RPE1 PRC1-GFP cell line; N = 33 control cells and 38 HAUS6-depleted cells following MG-132 treatment of the HeLa PRC1-GFP cell line; N = 31 control cells, 31 HAUS6-depleted cells following MG-132 treatment of the RPE1 CENP-A-GFP Centrin1-GFP cell line; N = 10 control, HAUS6- and HAUS8-depleted HeLa PRC1-GFP and RPE1 CENP-A-GFP Centrin1-GFP cells. (K) Overlap length measured in the side view of the spindle of control (gray) and HAUS6-depleted (yellow) RPE1 cells stably expressing PRC1-GFP and treated with MG-132 (left). N = 72 overlaps in 32 control cells and 74 overlaps in 39 HAUS6-depleted cells. Overlap length measured in the side view of the spindle of control (gray) and HAUS6-depleted (yellow) HeLa cells stably expressing PRC1-GFP and treated with MG-132 (middle, left). N = 96 overlaps in 33 control cells and 90 overlaps in 39 HAUS6-depleted cells. Overlap length measured in the side view of the spindle of control (gray) and HAUS6-depleted (yellow) cells immunostained for PRC1 without MG-132 treatment (middle, right). N = 27 overlaps in 10 control cells and 23 overlaps in 10 HAUS6-depleted cells. Overlap length measured in the side view of the spindle of control (gray), HAUS6- (yellow) and HAUS8-depleted (orange) HeLa cells stably expressing PRC1-GFP without MG-132 treatment (right). N = 50 overlaps in 10 cells for each condition. Each color in the plot corresponds to data obtained from one cell. (L) Univariate scatter plot of an overlap length divided by spindle length in control (gray) and HAUS6-depleted (yellow) HeLa cells stably expressing PRC1-GFP and treated with MG-132.

N = 96 overlaps in 33 control cells and 90 overlaps in 39 HAUS6-depleted cells. (M) Univariate scatter plot of an average overlap length divided by spindle length in control (gray), HAUS6- (yellow) and HAUS8-depleted (orange) HeLa cells stably expressing PRC1-GFP. N = 10 overlaps in 10 cells for each condition. (D, E, G, J-M) Boxes represent standard deviation (dark gray), 95% confidence interval of the mean (light gray) and mean value (black). All results were obtained from three independent experiments. Statistical analysis (C, G and L) Mann-Whitney U test; (E, J left panels, M) ANOVA with post-hoc Tukey test; (J and K) t-test for samples that followed normal distribution or Mann–Whitney U test for samples that significantly departured from normality, determined using the Shapiro-Wilk test; p-value legend: < 0.0001 (****), 0.0001 to 0.001 (***), 0.001 to 0.01 (**), 0.01 to 0.05 (*), ≥ 0.05 (ns). Scale bars, 2 µm.

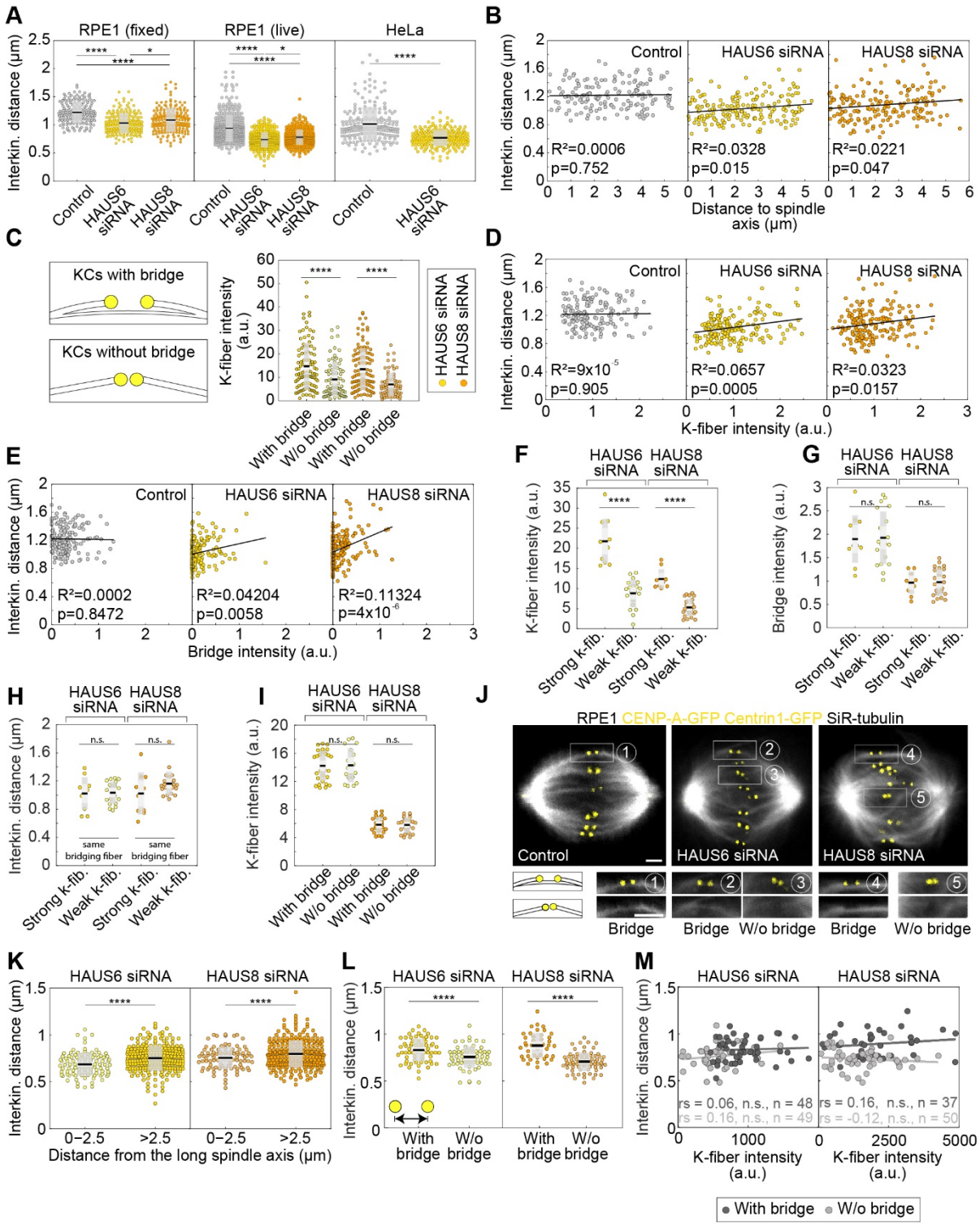


**Supplementary Figure 5 (S5).** (A) Univariate scatter plot of the interkinetochore distance in control (gray), HAUS6- (yellow) and HAUS8-depleted (orange) RPE1 cells stably expressing CENP-A-GFP and immunostained for α-tubulin (left). N = 158 kinetochore pairs in 30 control cells and 180 kinetochore pairs in 30 HAUS6- and HAUS8-depleted cells. Univariate scatter plot of the interkinetochore distance in control (gray), HAUS6- (yellow) and HAUS8-depleted (orange) RPE1 cells stably expressing CENP-A-GFP and Centrin1-GFP and stained with SiR-tubulin (middle). N = 446 kinetochore pairs in 10 control cells, 356 kinetochore pairs in 10 HAUS6-depleted cells, and 374 kinetochore pairs in 30 HAUS8-depleted cells. Univariate

scatter plot of the interkinetochore distance in control (gray) and HAUS6-depleted (yellow) HeLa cells stably expressing CENP-A-GFP and Centrin1-GFP and stained with SiR-tubulin (right). N = >100 kinetochore pairs in 5 control and HAUS6-depleted cells. (B) Correlation of the interkinetochore distance and distance to spindle axis in control (gray), HAUS6- (yellow) and HAUS8-depleted (orange) RPE1 cells stably expressing CENP-A-GFP and immunostained for α-tubulin. (C) Univariate scatter plots of the k-fiber intensity for kinetochore pairs with bridging fiber (dark colors) and without bridging fiber (light colors) in HAUS6- (yellow) and HAUS8-depleted (orange) RPE1 cells stably expressing CENP-A-GFP and immunostained for α-tubulin. Schematic representation of kinetochore pair (KCs) with and without bridging fiber (See Results). N = 30 HAUS6-depleted cells with 106 kinetochore pairs with bridging fibers and 74 kinetochore pairs without bridging fibers. N = 30 HAUS8-depleted cells with 110 kinetochore pairs with bridging fibers and 70 kinetochore pairs without bridging fibers. (D) Correlation of the interkinetochore distance and k-fiber intensity for kinetochore pairs in control (gray), HAUS6- (yellow) and HAUS8- (orange) depleted RPE1 cells stably expressing CENP-A-GFP and immunostained for α-tubulin. (E) Correlation of the interkinetochore distance and bridging fiber intensity for kinetochore pairs in control (gray), HAUS6- (yellow) and HAUS8- (orange) depleted RPE1 cells stably expressing CENP-A-GFP and immunostained for α-tubulin. (B, D and E) N = 158, 180 and 180 kinetochore pairs in 30 control, HAUS6- and HAUS8-depleted cells, respectively. (F) Univariate scatter plots of the k-fiber intensity for kinetochore pairs with stronger k-fiber (dark colors) and with weaker k-fiber (light colors) within subgroups of kinetochore pairs with or without bridging fiber after HAUS6 (yellow) or HAUS8 (orange) depletion in RPE1 cells stably expressing CENP-A-GFP and immunostained for α-tubulin. (G) Univariate scatter plots of the bridging fiber intensity of kinetochore pairs in (F). (H) Univariate scatter plots of the interkinetochore distance for kinetochore pairs in (F). (F-I) N = 11 kinetochore pairs with stronger k-fiber and 20 kinetochore pairs with weaker k-fiber in 30 HAUS6-depleted cells. N = 10 kinetochore pairs with stronger k-fiber and 23 kinetochore pairs with weaker k-fiber in 30 HAUS8-depleted cells. (I) Univariate scatter plot of the k-fiber intensity for kinetochore pairs with bridging fibers (dark colors) and without bridging fibers (light colors), after HAUS6 (yellow) or HAUS8 (orange) depletion in RPE1 cells stably expressing CENP-A-GFP and immunostained for α-tubulin. K-fiber intensities are chosen to be similar within the subgroups with or without a bridging fiber to exclude the contribution of k-fibers. N = 27 kinetochore pairs with a bridging fiber and 18 kinetochore pairs without a bridging fiber in HAUS6-depleted cells. N = 23 kinetochore pairs with a bridging fiber and 25 kinetochore pairs without a bridging fiber in HAUS8-depleted cells. (J) Live images (single z-plane) of metaphase spindles in RPE1 cells stably expressing CENP-A-GFP and Centrin1-GFP (both in yellow) and stained with SiR-tubulin (gray). Enlarged boxes show kinetochore (KC) pairs with or without a bridging fiber. All images are adjusted for clarity. Scale bars, 2 µm. (K) Univariate scatter plot of the interkinetochore distance in HAUS6- (yellow) or HAUS8- (orange) depleted cells depending on the 3D-distance from the long spindle axis. N = 10 HAUS6-depleted cells with 97 and 259 kinetochore pairs in the intervals of 0-2.5 and >2.5, respectively. N = 10 HAUS8-depleted cells with 95 and 265 kinetochore pairs in the interval of 0-2.5 and >2.5, respectively. (L) Univariate scatter plot of the interkinetochore distance in HAUS6- (yellow) and HAUS8- (orange) depleted cells. N = 10 cells with >50 kinetochore pairs. Kinetochore pairs are divided into two groups: with bridging fiber (dark gray) and without bridging fiber (light gray). N = 65 kinetochore pairs with and without a bridging fiber in 10 HAUS6-depleted cells; N = 42 kinetochore pairs with a bridging fiber and 74 kinetochore pairs without a bridging fiber in HAUS8-depleted cells. (M)

Correlation of the interkinetochore distance and k-fiber intensity for kinetochore pairs with (dark gray) and without (light gray) a bridging fiber in HAUS6 siRNA (left) and HAUS8 siRNA (right)-treated cells. The data represent a subset from L, in which only kinetochore pairs with k-fibers well isolated from neighboring microtubules were taken into account. The interkinetochore distance values for kinetochore pairs with and without bridging fibers were 0.83 ± 0.02 and 0.76 ± 0.02 µm for HAUS6 siRNA- and 0.89 ± 0.02 and 0.73 ± 0.01 µm for HAUS8 siRNA-treated cells, respectively, in agreement with results from panel L. rs, Spearman correlation coefficient. (A, C, F-I, K, L) Boxes represent standard deviation (dark gray), 95% confidence interval of the mean (light gray) and mean value (black). All results were obtained from three independent experiments. Statistical analysis (A left and middle) ANOVA with post-hoc Tukey test; (A right) t-test; (B, D, E and M) linear regression; (C, F-I, K and L) t-test for samples that followed normal distribution or Mann–Whitney U test for samples that significantly departured from normality, determined using the Shapiro-Wilk test; p-value legend: < 0.0001 (****), 0.0001 to 0.001 (***), 0.001 to 0.01 (**), 0.01 to 0.05 (*), ≥ 0.05 (ns).

**Supplementary Video 1.** RPE1 cells stably expressing CENP-A-GFP and Centrin1-GFP (16-colors) following Mad2 depletion. Kinetochores are color-coded for depth from blue to red with the 16 Colors LUT and noise was processed with the Despeckle function in ImageJ. Scale bar, 2 µm.

**Supplementary Video 2.** RPE1 cells stably expressing CENP-A-GFP and Centrin1-GFP (16-colors) following Mad2/HAUS6 depletion. Kinetochores are color-coded for depth from blue to red with the 16 Colors LUT and noise was processed with the Despeckle function in ImageJ. Scale bar, 2 µm.

## REFERENCES


Almeida, A.C., J. Soares-de-Oliveira, D. Drpic, L.P. Cheeseman, J. Damas, H.A. Lewin, D.M. Larkin, P. Aguiar, A.J. Pereira, and H. Maiato. 2022. Augmin-dependent microtubule self-organization drives kinetochore fiber maturation in mammals. *Cell Reports*. 39:110610. doi:10.1016/j.celrep.2022.110610.

Asthana, J., N.I. Cade, D. Normanno, W.M. Lim, and T. Surrey. 2021. Gradual compaction of the central spindle decreases its dynamicity in PRC1 and EB1 gene-edited cells. *Life Sci. Alliance*. 4:e202101222. doi:10.26508/lsa.202101222.

Brust-Mascher, I., P. Sommi, D.K. Cheerambathur, and J.M. Scholey. 2009. Kinesin-5-dependent poleward flux and spindle length control in Drosophila embryo mitosis. *Mol Biol Cell*. 20:1749–1762. doi:10.1091/mbc.e08-10-1033.

Buđa, R., K. Vukušić, and I.M. Tolić. 2017. Dissection and characterization of microtubule bundles in the mitotic spindle using femtosecond laser ablation. *In* Methods in Cell Biology. T. Lecuit, editor. Academic Press. 81–101.

Cerami, E., J. Gao, U. Dogrusoz, B.E. Gross, S.O. Sumer, B.A. Aksoy, A. Jacobsen, C.J. Byrne, M.L. Heuer, E. Larsson, Y. Antipin, B. Reva, A.P. Goldberg, C. Sander, and N. Schultz. 2012. The cBio cancer genomics portal: an open platform for exploring multidimensional cancer genomics data. *Cancer Discov*. 2:401–404. doi:10.1158/2159-8290.CD-12-0095.

David, A.F., P. Roudot, W.R. Legant, E. Betzig, G. Danuser, and D.W. Gerlich. 2019. Augmin accumulation on long-lived microtubules drives amplification and kinetochore-directed growth. *J Cell Biol*. 218:2150–2168. doi:10.1083/jcb.201805044.

DeLuca, J.G., W.E. Gall, C. Ciferri, D. Cimini, A. Musacchio, and E.D. Salmon. 2006. Kinetochore microtubule dynamics and attachment stability are regulated by Hec1. *Cell*. 127:969–982. doi:10.1016/j.cell.2006.09.047.

Dudka, D., A. Noatynska, C.A. Smith, N. Liaudet, A.D. McAinsh, and P. Meraldi. 2018. Complete microtubule–kinetochore occupancy favours the segregation of merotelic attachments. *Nat Commun*. 9:2042. doi:10.1038/s41467-018-04427-x.

Ganem, N.J., K. Upton, and D.A. Compton. 2005. Efficient mitosis in human cells lacking poleward microtubule flux. *Curr Biol*. 15:1827–1832. doi:10.1016/j.cub.2005.08.065.

Gao, J., B.A. Aksoy, U. Dogrusoz, G. Dresdner, B. Gross, S.O. Sumer, Y. Sun, A. Jacobsen, R. Sinha, E. Larsson, E. Cerami, C. Sander, and N. Schultz. 2013. Integrative analysis of complex cancer genomics and clinical profiles using the cBioPortal. *Sci Signal*. 6:pl1. doi:10.1126/scisignal.2004088.

Goshima, G., M. Mayer, N. Zhang, N. Stuurman, and R.D. Vale. 2008. Augmin: a protein complex required for centrosome-independent microtubule generation within the spindle. *J Cell Biol*. 181:421–429. doi:10.1083/jcb.200711053.

Goshima, G., R. Wollman, S.S. Goodwin, N. Zhang, J.M. Scholey, R.D. Vale, and N. Stuurman. 2007. Genes required for mitotic spindle assembly in Drosophila S2 cells. *Science*. 316:417–421. doi:10.1126/science.1141314.

Hayward, D., J. Metz, C. Pellacani, and J.G. Wakefield. 2014. Synergy between multiple microtubule-generating pathways confers robustness to centrosome-driven mitotic spindle formation. *Dev Cell*. 28:81–93. doi:10.1016/j.devcel.2013.12.001.

Hell, S.W., and J. Wichmann. 1994. Breaking the diffraction resolution limit by stimulated emission: stimulated-emission-depletion fluorescence microscopy. *Opt Lett*. 19:780–782. doi:10.1364/ol.19.000780.

Jagrić, M., P. Risteski, J. Martinčić, A. Milas, and I.M. Tolić. 2021. Optogenetic control of PRC1 reveals its role in chromosome alignment on the spindle by overlap length-dependent forces. *eLife*. 10:e61170. doi:10.7554/eLife.61170.

Kajtez, J., A. Solomatina, M. Novak, B. Polak, K. Vukušić, J. Rüdiger, G. Cojoc, A. Milas, I. Šumanovac Šestak, P. Risteski, F. Tavano, A.H. Klemm, E. Roscioli, J. Welburn, D. Cimini, M. Glunčić, N. Pavin, and I.M. Tolić. 2016. Overlap microtubules link sister k-fibres and balance the forces on bi-oriented kinetochores. *Nat Commun*. 7:10298. doi:10.1038/ncomms10298.

Kamasaki, T., E. O'Toole, S. Kita, M. Osumi, J. Usukura, J.R. McIntosh, and G. Goshima. 2013. Augmin-dependent microtubule nucleation at microtubule walls in the spindle. *J Cell Biol*. 202:25–33. doi:10.1083/jcb.201304031.

Kiewisz, R., G. Fabig, W. Conway, D. Baum, D. Needleman, and T. Muller-Reichert. 2022. Three-dimensional structure of the kinetochore-fibers in human mitotic spindles. *bioRxiv*. doi:10.1101/2021.11.13.468347. (Preprint posted July 17, 2022).

Kirschner, M., and T. Mitchison. 1986. Beyond self-assembly: From microtubules to morphogenesis. *Cell*. 45:329–342. doi:10.1016/0092-8674(86)90318-1.

Klar, T.A., and S.W. Hell. 1999. Subdiffraction resolution in far-field fluorescence microscopy. *Opt Lett*. 24:954–956. doi:10.1364/ol.24.000954.

Lampson, M.A., and E.L. Grishchuk. 2017. Mechanisms to Avoid and Correct Erroneous Kinetochore-Microtubule Attachments. *Biology (Basel)*. 6:E1. doi:10.3390/biology6010001.

Lawo, S., M. Bashkurov, M. Mullin, M.G. Ferreria, R. Kittler, B. Habermann, A. Tagliaferro, I. Poser, J.R.A. Hutchins, B. Hegemann, D. Pinchev, F. Buchholz, J.-M. Peters, A.A. Hyman, A.-C. Gingras, and L. Pelletier. 2009. HAUS, the 8-subunit human Augmin complex, regulates centrosome and spindle integrity. *Curr Biol*. 19:816–826. doi:10.1016/j.cub.2009.04.033.

Li, J., M. Dallmayer, T. Kirchner, J. Musa, and T.G.P. Grünewald. 2018. PRC1: Linking Cytokinesis, Chromosomal Instability, and Cancer Evolution. *Trends Cancer*. 4:59–73. doi:10.1016/j.trecan.2017.11.002.

Lukinavičius, G., L. Reymond, E. D'Este, A. Masharina, F. Göttfert, H. Ta, A. Güther, M. Fournier, S. Rizzo, H. Waldmann, C. Blaukopf, C. Sommer, D.W. Gerlich, H.-D. Arndt, S.W. Hell, and K. Johnsson. 2014. Fluorogenic probes for live-cell imaging of the cytoskeleton. *Nat Methods*. 11:731–733. doi:10.1038/nmeth.2972.

Maiato, H., C.L. Rieder, and A. Khodjakov. 2004. Kinetochore-driven formation of kinetochore fibers contributes to spindle assembly during animal mitosis. *J Cell Biol*. 167:831–840. doi:10.1083/jcb.200407090.

Mastronarde, D.N., K.L. McDonald, R. Ding, and J.R. McIntosh. 1993. Interpolar spindle microtubules in PTK cells. *J Cell Biol*. 123:1475–1489. doi:10.1083/jcb.123.6.1475.

Matković, J., S. Ghosh, M. Ćosić, M. Barišić, N. Pavin, and I.M. Tolić. 2022. Kinetochore- and chromosome-driven transition of microtubules into bundles promotes spindle assembly. *bioRxiv*. doi:10.1101/2022.02.25.481924. (Preprint posted March 02, 2022).

Mayr, M.I., S. Hümmer, J. Bormann, T. Grüner, S. Adio, G. Woehlke, and T.U. Mayer. 2007. The human kinesin Kif18A is a motile microtubule depolymerase essential for chromosome congression. *Curr Biol*. 17:488–498. doi:10.1016/j.cub.2007.02.036.

McDonald, K.L., E.T. O'Toole, D.N. Mastronarde, and J.R. McIntosh. 1992. Kinetochore microtubules in PTK cells. *J Cell Biol*. 118:369–383. doi:10.1083/jcb.118.2.369.

McIntosh, J.R. 2016. Mitosis. *Cold Spring Harb Perspect Biol*. 8:a023218. doi:10.1101/cshperspect.a023218.

Mitchison, T. j. 2005. Mechanism and function of poleward flux in Xenopus extract meiotic spindles. *Philosophical Transactions of the Royal Society B: Biological Sciences*. 360:623–629. doi:10.1098/rstb.2004.1616.

Miyamoto, D.T., Z.E. Perlman, K.S. Burbank, A.C. Groen, and T.J. Mitchison. 2004. The kinesin Eg5 drives poleward microtubule flux in Xenopus laevis egg extract spindles. *J Cell Biol*. 167:813–818. doi:10.1083/jcb.200407126.

Mollinari, C., J.-P. Kleman, W. Jiang, G. Schoehn, T. Hunter, and R.L. Margolis. 2002. PRC1 is a microtubule binding and bundling protein essential to maintain the mitotic spindle midzone. *J Cell Biol*. 157:1175–1186. doi:10.1083/jcb.200111052.

Musacchio, A., and E.D. Salmon. 2007. The spindle-assembly checkpoint in space and time. *Nat Rev Mol Cell Biol*. 8:379–393. doi:10.1038/nrm2163.

Nicklas, R.B., S.C. Ward, and G.J. Gorbsky. 1995. Kinetochore chemistry is sensitive to tension and may link mitotic forces to a cell cycle checkpoint. *J Cell Biol*. 130:929–939. doi:10.1083/jcb.130.4.929.

Novak, M., B. Polak, J. Simunić, Z. Boban, B. Kuzmić, A.W. Thomae, I.M. Tolić, and N. Pavin. 2018. The mitotic spindle is chiral due to torques within microtubule bundles. *Nat Commun*. 9:3571. doi:10.1038/s41467-018-06005-7.

O'Toole, E., M. Morphew, and J.R. McIntosh. 2020. Electron tomography reveals aspects of spindle structure important for mechanical stability at metaphase. *MBoC*. 31:184–195. doi:10.1091/mbc.E19-07-0405.

Pavin, N., and I.M. Tolić. 2016. Self-Organization and Forces in the Mitotic Spindle. *Annu Rev Biophys*. 45:279–298. doi:10.1146/annurev-biophys-062215-010934.

Petry, S. 2016. Mechanisms of Mitotic Spindle Assembly. *Annu Rev Biochem*. 85:659–683. doi:10.1146/annurev-biochem-060815-014528.

Petry, S., A.C. Groen, K. Ishihara, T.J. Mitchison, and R.D. Vale. 2013. Branching microtubule nucleation in Xenopus egg extracts mediated by augmin and TPX2. *Cell*. 152:768–777. doi:10.1016/j.cell.2012.12.044.

Petry, S., C. Pugieux, F.J. Nédélec, and R.D. Vale. 2011. Augmin promotes meiotic spindle formation and bipolarity in Xenopus egg extracts. *Proc Natl Acad Sci U S A*. 108:14473–14478. doi:10.1073/pnas.1110412108.

Polak, B., P. Risteski, S. Lesjak, and I.M. Tolić. 2017. PRC1-labeled microtubule bundles and kinetochore pairs show one-to-one association in metaphase. *EMBO Rep*. 18:217–230. doi:10.15252/embr.201642650.

Prosser, S.L., and L. Pelletier. 2017. Mitotic spindle assembly in animal cells: a fine balancing act. *Nat Rev Mol Cell Biol*. 18:187–201. doi:10.1038/nrm.2016.162.

Risteski, P., D. Božan, M. Jagrić, A. Bosilj, N. Pavin, and I.M. Tolić. 2021. Coordinated poleward flux of sister kinetochore fibers drives chromosome alignment. *bioRxiv*. doi:10.1101/2020.12.30.424837. (Preprint posted July 24, 2021)

Sacristan, C., M.U.D. Ahmad, J. Keller, J. Fermie, V. Groenewold, E. Tromer, A. Fish, R. Melero, J.M. Carazo, J. Klumperman, A. Musacchio, A. Perrakis, and G.J. Kops. 2018. Dynamic kinetochore size regulation promotes microtubule capture and chromosome biorientation in mitosis. *Nat Cell Biol*. 20:800–810. doi:10.1038/s41556-018-0130-3.

Sen, O., J.U. Harrison, N.J. Burroughs, and A.D. McAinsh. 2021. Kinetochore life histories reveal an Aurora-B-dependent error correction mechanism in anaphase. *Developmental Cell*. 56:3082-3099.e5. doi:10.1016/j.devcel.2021.10.007.

Sikirzhytski, V., F. Renda, I. Tikhonenko, V. Magidson, B.F. McEwen, and A. Khodjakov. 2018. Microtubules assemble near most kinetochores during early prometaphase in human cells. *Journal of Cell Biology*. 217:2647–2659. doi:10.1083/jcb.201710094.

Silkworth, W.T., I.K. Nardi, R. Paul, A. Mogilner, and D. Cimini. 2011. Timing of centrosome separation is important for accurate chromosome segregation. *MBoC*. 23:401–411. doi:10.1091/mbc.e11-02-0095.

Song, J.-G., M.R. King, R. Zhang, R.S. Kadzik, A. Thawani, and S. Petry. 2018. Mechanism of how augmin directly targets the γ-tubulin ring complex to microtubules. *J Cell Biol*. 217:2417–2428. doi:10.1083/jcb.201711090.

Steblyanko, Y., G. Rajendraprasad, M. Osswald, S. Eibes, A. Jacome, S. Geley, A.J. Pereira, H. Maiato, and M. Barisic. 2020. Microtubule poleward flux in human cells is driven by the coordinated action of four kinesins. *EMBO J*. 39:e105432. doi:10.15252/embj.2020105432.

Tolić, I.M., and N. Pavin. 2016. Bridging the gap between sister kinetochores. *Cell Cycle*. 15:1169–1170. doi:10.1080/15384101.2016.1157976.

Tulu, U.S., C. Fagerstrom, N.P. Ferenz, and P. Wadsworth. 2006. Molecular requirements for kinetochore-associated microtubule formation in mammalian cells. *Curr Biol*. 16:536–541. doi:10.1016/j.cub.2006.01.060.

Uehara, R., and G. Goshima. 2010. Functional central spindle assembly requires de novo microtubule generation in the interchromosomal region during anaphase. *J Cell Biol*. 191:259–267. doi:10.1083/jcb.201004150.

Uehara, R., T. Kamasaki, S. Hiruma, I. Poser, K. Yoda, J. Yajima, D.W. Gerlich, and G. Goshima. 2016. Augmin shapes the anaphase spindle for efficient cytokinetic furrow ingression and abscission. *Mol Biol Cell*. 27:812–827. doi:10.1091/mbc.E15-02-0101.

Uehara, R., R. Nozawa, A. Tomioka, S. Petry, R.D. Vale, C. Obuse, and G. Goshima. 2009. The augmin complex plays a critical role in spindle microtubule generation for mitotic progression and cytokinesis in human cells. *Proc Natl Acad Sci U S A*. 106:6998–7003. doi:10.1073/pnas.0901587106.

Verma, V., and T.J. Maresca. 2019. Direct observation of branching MT nucleation in living animal cells. *J Cell Biol*. 218:2829–2840. doi:10.1083/jcb.201904114.

Viais, R., M. Fariña-Mosquera, M. Villamor-Payà, S. Watanabe, L. Palenzuela, C. Lacasa, and J. Lüders. 2021. Augmin deficiency in neural stem cells causes p53-dependent apoptosis and aborts brain development. *Elife*. 10:e67989. doi:10.7554/eLife.67989.

Vukušić, K., R. Buđa, A. Bosilj, A. Milas, N. Pavin, and I.M. Tolić. 2017. Microtubule Sliding within the Bridging Fiber Pushes Kinetochore Fibers Apart to Segregate Chromosomes. *Dev Cell*. 43:11-23.e6. doi:10.1016/j.devcel.2017.09.010.

Waters, J.C., R.V. Skibbens, and E.D. Salmon. 1996. Oscillating mitotic newt lung cell kinetochores are, on average, under tension and rarely push. *J Cell Sci*. 109:2823–2831. doi:10.1242/jcs.109.12.2823.

Wu, G., Y.-T. Lin, R. Wei, Y. Chen, Z. Shan, and W.-H. Lee. 2008. Hice1, a novel microtubule-associated protein required for maintenance of spindle integrity and chromosomal stability in human cells. *Mol Cell Biol*. 28:3652–3662. doi:10.1128/MCB.01923-07.

Zhu, H., J.A. Coppinger, C.-Y. Jang, J.R. Yates, and G. Fang. 2008. FAM29A promotes microtubule amplification via recruitment of the NEDD1-gamma-tubulin complex to the mitotic spindle. *J Cell Biol*. 183:835–848. doi:10.1083/jcb.200807046.